Numerical study of drop motion on a surface with stepwise wettability gradient and contact angle hysteresis

Jun-Jie Huang, Haibo Huang, and Xinzhu Wang

Articles you may be interested in

A numerical approach for the direct computation of flows including fluid-solid interaction: Modeling contact angle, film rupture, and dewetting
Phys. Fluids **28**, 062002 (2016); 10.1063/1.4949522

Multiscale liquid drop impact on wettable and textured surfaces
Phys. Fluids **26**, 082003 (2014); 10.1063/1.4892083

Experimental study on macroscopic contact line behaviors during bubble formation on submerged orifice and comparison with numerical simulations
Phys. Fluids **25**, 092105 (2013); 10.1063/1.4821043

Droplet spreading on a porous surface: A lattice Boltzmann study
Phys. Fluids **24**, 042101 (2012); 10.1063/1.3701996

Wetting gradient induced separation of emulsions: A combined experimental and lattice Boltzmann computer simulation study
Phys. Fluids **20**, 072104 (2008); 10.1063/1.2963958

Numerical study of drop motion on a surface with stepwise wettability gradient and contact angle hysteresis

Jun-Jie Huang,[1,2,3,a)] Haibo Huang,[4] and Xinzhu Wang[1,2]
[1]*Department of Engineering Mechanics, Chongqing University, Chongqing 400044, China*
[2]*Chongqing Key Laboratory of Heterogeneous Material Mechanics (Chongqing University), Chongqing 400044, China*
[3]*State Key Laboratory of Mechanical Transmission, Chongqing University, Chongqing 400044, China*
[4]*Department of Modern Mechanics, University of Science and Technology of China, Hefei, Anhui 230026, China*

In this work, the motion of a two-dimensional drop on a surface with stepwise wettability gradient (WG) is studied numerically by a hybrid lattice-Boltzmann finite-difference method. We incorporate the geometric wetting boundary condition that allows accurate implementation of a contact angle hysteresis (CAH) model. The method is first validated through a series of tests that check different constituents of the numerical model. Then, simulations of a drop on a wall with given stepwise WG are performed under different conditions. The effects of the Reynolds number, the viscosity ratio, the WG, as well as the CAH on the drop motion are investigated in detail. It was discovered that the shape of the drop in steady motion may be fitted by two arcs that give two apparent contact angles, which are related to the respective contact line velocities and the relevant contact angles (that specify the WG and CAH) through the relation derived by Cox ["The dynamics of the spreading of liquids on a solid surface. Part 1. viscous flow," J. Fluid Mech. **168**, 169–194 (1986)] if the slip length in simulation is defined according to Yue *et al.* ["Sharp-interface limit of the Cahn-Hilliard model for moving contact lines," J. Fluid Mech. **645**, 279–294 (2010)]. It was also found that the steady capillary number of the drop is significantly affected by the viscosity ratio, the magnitudes of the WG, and the CAH, whereas it almost shows no dependence on the Reynolds number. © *2014 AIP Publishing LLC*. [http://dx.doi.org/10.1063/1.4880656]

I. INTRODUCTION

The motion of a drop is encountered in nature, in our daily life, and in many industries as well. It may be caused by body forces such as gravity, by a difference in pressure, or by a difference in surface forces (for example, the Marangoni effect due to surface tension gradient and a migrating drop on a surface with wettability gradient (WG)). As the size of the drop decreases, the surface forces become more important in determining the motion of the drop. To drive and control the motion of discrete drops through modifications of surface wettability possesses many advantages at small scales. Such problems have received more and more attention in recent years because of their significance in digital microfluidics and the development of lab-on-a-chip as well as some other technologies.[1] For instance, recently, Lai, Hsu, and Yang[2] employed a surface with WG to accelerate a droplet before its collision with another one to enhance the mixing between them, and Bardaweel *et al.*[3] developed a micropump by using axisymmetric WG to drive droplets, which has potential applications in some microelectromechanical systems. Besides, gradient surfaces or

---

a)Authors to whom correspondence should be addressed. Electronic addresses: jjhuang1980@gmail.com and jjhuang@cqu.edu.cn.

    26, 062101-1

directional surfaces, including those having WG, have been found to be used for droplet transport in many natural phenomena.[4] Therefore, the study of drop motion caused by WG has important implications in many areas. Due to the presence of either geometrical or chemical heterogeneities (or both), the motion of an interface on solid substrates usually shows certain hysteresis, i.e., the contact angle when the interface is moving forward (called the *advancing contact angle*, denoted as θ_A) is larger than that when it is moving backward (called the *receding contact angle*, denoted as θ_R). This phenomenon is known as contact angle hysteresis (CAH). It is characterized by the difference between the two angles, $\theta_A - \theta_R$, and it may strongly affect a drop driven by WG especially at small scales.

The study of drops under WG began more than two decades ago. Previous studies on this topic include theoretical and numerical modelling, experimental investigations and the combination of both. Brochard[5] analyzed the motion of two-dimensional (2D) and three-dimensional (3D) droplets on substrates with small gradient in wettability or temperature at different scales and obtained the formula for the droplet velocity through the balance of driving and resistance forces under the quasi-steady assumption as well as some other simplifying assumptions. By employing the wedge and lubrication approximations respectively, Subramanian, Moumen, and McLaughlin[6] derived two sets of approximate results for a 3D drop driven by WG on the resistance acting on the drop and also on the quasi-steady drop velocity. Pismen and Thiele[7] developed an asymptotic theory for a WG-driven 2D droplet based on the lubrication analysis. The droplet's shape and velocity were obtained as functions of the WG and the volume of the droplet. Halverson *et al.*[8] carried out molecular dynamics (MD) study of the dynamics of a nanodroplet on a surface with different types of WG. Systems of nanometer scale, including a Lennard-Jones system and water on a self-assembled monolayer, were investigated and the observables reported by Halverson *et al.*[8] included the shape, the center-of-mass position, the velocity, the base length, and the advancing and receding angles of the droplet during the motion. Reasonable agreement were obtained between the MD simulation and theoretical prediction on the droplet velocity. Considerable focus was given by Halverson *et al.*[8] to the CAH, the inclusion of which improved the agreement. It is noted that the work by Halverson *et al.*[8] may be regarded as (virtual) experiment and there were no explicit CAH model because of the extremely small size. Huang, Shu, and Chew[9] performed 3D simulations using the lattice Boltzmann method (LBM) of a droplet on substrates with different wettability distribution and temporal control (of the wettability), and identified suitable spatiotemporal wettability control parameters for unidirectional droplet transport. Recently, Shi, Hu, and Zhou[10] employed LBM to simulate a 2D droplet on a substrate with a step WG, which was set to follow the droplet's motion to ensure a continually acting driving force (to some extent, mimicking the situation of reactive wetting used in Ref. 11). Variations of the droplet velocity and the dynamic contact angles were extracted from the simulations and were shown to agree reasonably well with theoretical predictions when the WG was small. Das and Das[12] employed the smoothed particle hydrodynamics technique based on the diffuse interface method to study the dynamics of a 3D drop on an inclined surface with WG. The effects of the drop size, the angle of surface inclination, and the strength of WG on the drop motion were investigated, and several possible outcomes were reported, depending on these conditions. Das and Das[12] presented some results about CAH for the drop even though they did not introduce any surface heterogeneities or use any explicit CAH model (thus we suspect that the reported CAH is actually due to some dynamic effects or simply reflects the interaction between the gravity and WG, and is not like the CAH in other studies). Xu and Qian[13] presented systematically a phase-field-based thermohydrodynamic model for one-component two-phase fluids with certain boundary conditions derived from various balance equations, and employed it to numerically study the 2D droplet motion on substrates having given WG with/without phase transition and substrate temperature change. They investigated the droplet's shape, migration velocity V_{mig}, the velocity profile at selected sections, and the distribution of slip velocity. They obtained the relations between V_{mig}, the magnitude of WG (denoted by $S_{\text{wg}} = \frac{d}{dx}\cos\theta$ where θ is the contact angle of the wall and x is the coordinate along the direction of WG) and the slip length l_s, which agree with previous theoretical predictions by Brochard.[5] The effects of CAH were not considered by Xu and Qian,[13] which makes the $V_{\text{mig}} - S_{\text{wg}}$ line pass the origin (in the presence of CAH, V_{mig} may remain to be zero before S_{wg} reaches certain minimum value capable of driving the droplet). Esmaili, Moosavi, and Mazloomi[14] carried out LBM simulations of a 2D droplet inside

a microchannel with a stepwise change in wettability, which differs from most of previous studies on droplets under open geometry. The simulated evolutions of the droplet velocity were found to agree well with analytical predictions developed by Esmaili, Moosavi, and Mazloomi.[14] They focused on the effects of the channel height, the ratios of fluid viscosity and density, the channel geometry (for grooved channels), as well as the appearance of an obstacle inside the channel.

In addition to the above theoretical and numerical studies, there is also some experimental work in this field, which motivated some of the above investigations. Ondarcuhu and Veyssie[15] did experimental studies about the dynamics of a 2D drop (liquid ridge) sitting across a wettability discontinuity. The displacements and constant angles of the two contact lines of the drop were measured and several stages of motion were identified, including a steady stage with constant velocity and constant advancing and receding angles. Chaudhury and Whitesides[16] demonstrated the (continuous) WG-driven (water) drop in experiment even on a substrate tilted to the horizontal by 15°, showing that the driving force caused by a strong chemical gradient can become large enough to overcome both the gravity and the hydrodynamic resistance. They also pointed out that the effect of CAH must be small; otherwise, the drop might not move. Santos and Ondarcuhu[11] demonstrated spontaneous droplet motion on a surface that is modified by some agents inside the droplet through some reaction. A quite broad range of droplet velocities were reported, and the relations between the droplet velocity and its size as well as the receding contact angle were obtained and compared favorably with the theoretical ones. To guide the droplet's motion, a track between two hydrophobic regions was employed by Santos and Ondarcuhu.[11] Moumen, Subramanian, and McLaughlin[17] reported experiments for a 3D drop on a surface with spatially varying WG, and the respective results were compared with the theoretical predictions presented in Ref. 6 assuming quasi-steady state. The variations of the velocity of the drop with its position were obtained in the experiments. The theoretical results were shown to agree reasonably well with the experimental ones when the hysteresis effect was included, but larger discrepancy was seen if the hysteresis effect was not considered in the theoretical ones. Mo, Liu, and Kwok[18] employed reactive-wetting, which modifies the wetting property once a drop covers the surface, to drive a 3D drop along a (tilted) surface, and they reported the measured drop velocities at different angle of inclination. Besides, Mo, Liu, and Kwok[18] also performed computer simulations using LBM to visualize the drop motion, the flow, and pressure fields. Hysteresis effect was reported to be negligible because of the specifically selected and prepared gold substrates. Yamada and Tada[19] demonstrated reversible droplet transport through experiments that used dynamic bias voltage to adjust electrochemical reactions and ultimately to generate WG. Varnik *et al.*[20] did experimental studies on emulsion separation induced by an abrupt change in wettability and also did LBM simulations of a 3D droplet on a surface with a step WG. Enhanced separation was reported in confined geometry and it was also highlighted that smaller droplets are more easily guided by the step WG. In their simulations, the substrates were assumed to be ideally flat and the hysteresis effects did not come into play.

Besides various investigations on the WG-driven drop, there are also some studies exploring techniques to overcome the effects of CAH. Daniel and Chaudhury[21] showed that the resistance caused by CAH may be greatly reduced by applying a periodic force to the drop driven by a continuous WG generated from an in-plane vibration that resulted from an audio speaker. Later, Daniel *et al.*[22] extended this study to more fluids with different surface tensions and viscosities and explored the vibration parameters (including the wave form, amplitude and frequency). They found an interesting ratcheting motion of a drop on gradient surfaces that results from shape fluctuation and that the drop velocity increases linearly with the amplitude but nonlinearly with the frequency.

Despite abundant research on WG-driven drops there are still certain open questions and characteristics of such drop motions that remain to be explored. Most existing theoretical or numerical studies on WG-driven drops[7,9,10,12–14,18,20] have not included (explicitly) the effects of CAH through a *continuum* model even though CAH has been long identified as an important factor in the motion of WG-driven drop.[16,17] How CAH affects the migration velocity and the flow need to be investigated more thoroughly or to be further confirmed by simulations. In addition, the characteristics of the shape of a WG-driven drop in motion have been rarely studied. Although there are abundant studies on the relation between the shape of a moving interface, the contact angle and the contact line velocity

by using theoretical,[23,24] experimental,[25,26] and numerical methods,[26–28] most of them focused on either a simple interface or a drop spreading/dewetting on a surface. As far as we know, this kind of study is still lacking for WG-driven drops. Besides, most previous studies did not consider the effects of the surrounding fluid. This is reasonable for air-liquid systems with large density and viscosity contrasts, but may be questionable for liquid-liquid (e.g., water-oil) systems. Just for curiosity, it is also of interest to know how the surrounding fluid affects the drop motion caused by WG. In this work, we study a 2D drop on a surface with specified WG numerically by a phase-field-based hybrid LBM that incorporates a CAH model. Our aim is mainly to investigate the characteristics of the shape of a WG-driven drop (including its relation with the contact angles and velocities), and to explore the effects of the Reynolds number, the wettability gradient of different strengths, the viscosity ratio, and the CAH on the motion of the drop. Even though phenomenological CAH models have been included in simulations of various multiphase flows, including a drop subject to a shear flow, a pressure gradient or under the action of gravity (see, e.g., Refs. 29–34), it appears to us that they have not been used in the study of WG-driven drops. Thus, this work is a further and essential step towards more accurate and realistic simulations of WG-driven drops.

The paper is organized as follows. Section II introduces the phase-field model for binary fluids and the wetting boundary condition (WBC) on a wall together with the CAH model. The numerical method (simplified from Ref. 35) and the implementation of the WBC and CAH model are also described briefly in this section. In Sec. III, several validation tests are presented first and then investigations on a drop driven by a stepwise WG are carried out under different conditions, and the results are discussed and compared with some theoretical predictions as well as some other numerical studies. Finally, Sec. IV summaries the findings and concludes this paper.

II. THEORETICAL AND NUMERICAL METHODOLOGY

The present simulations are based on the phase-field modeling of two-phase flows. The physical governing equations are solved by a hybrid lattice-Boltzmann finite-difference method. For flows of binary fluids, there are two fundamental dynamics: the hydrodynamics for fluid flow and the interfacial dynamics. We introduce the phase-field model for interfacial dynamics first.

A. Phase-field model

In the phase-field model, two immiscible fluids are distinguished by an order parameter field ϕ. For a system of binary fluids, a free energy functional $\mathcal{F}$ may be defined based on ϕ as

$$\mathcal{F}(\phi, \nabla\phi) = \int_V \left(\Psi(\phi) + \frac{1}{2}\kappa|\nabla\phi|^2 \right) dV + \int_S \varphi(\phi_S)dS, \tag{1}$$

where $\Psi(\phi)$ is the *bulk free energy* density. The popular form of $\Psi(\phi)$ is the double-well form,

$$\Psi(\phi) = a(\phi^2 - 1)^2, \tag{2}$$

with a being a constant. With this form of $\Psi(\phi)$, ϕ varies between 1 in one of the fluids (named *fluid A* for convenience) and -1 in the other (named *fluid B*). The second term in the bracket on the right-hand side (RHS) of Eq. (1) is the *interfacial energy* density with κ being another constant, and the last term on the RHS of Eq. (1) in the surface integral, $\varphi(\phi_S)$, is the *surface energy* density with ϕ_S being the order parameter on the surface (i.e., solid wall).

The chemical potential μ is obtained by taking the variation of the free energy functional $\mathcal{F}$ with respect to the order parameter ϕ,

$$\mu = \frac{\delta\mathcal{F}}{\delta\phi} = \frac{d\Psi(\phi)}{d\phi} - \kappa\nabla^2\phi = 4a\phi(\phi^2 - 1) - \kappa\nabla^2\phi. \tag{3}$$

The coefficients a (in the bulk free energy) and κ (in the interfacial energy) are related to the interfacial tension σ and interface width W as[36]

$$a = \frac{3\sigma}{4W}, \quad \kappa = \frac{3\sigma W}{8}. \tag{4}$$

Equivalently, the interfacial tension σ and interface width W can be expressed in terms of a and κ as

$$\sigma = \frac{4}{3}\sqrt{2\kappa a}, \quad W = \sqrt{\frac{2\kappa}{a}}. \tag{5}$$

Usually, it is assumed that the diffusion of the order parameter is driven by the gradient of the chemical potential. By also including the contribution due to convection, one obtains the following evolution equation of the order parameter,[37]

$$\frac{\partial \phi}{\partial t} + (\boldsymbol{u} \cdot \nabla)\phi = \nabla \cdot (M\nabla\mu), \tag{6}$$

where M is the diffusion coefficient called *mobility* (taken as constant in this work), and $\boldsymbol{u}$ is the local fluid velocity.

Suitable boundary conditions are needed for Eqs. (3) and (6). Here we mainly focus on the conditions near a (rigid) wall, which are closely related to the wetting phenomenon and the motion of contact line. For the fluid velocity $\boldsymbol{u}$ that appears in Eq. (6), we assume that the no-slip condition applies on a wall. In what follows, we concentrate on the conditions for the phase-field variables, ϕ and μ. It is noted that in phase-field simulations interface slip on a wall is allowed due to the diffusion in Eq. (6).[38]

B. Wetting boundary condition

On a wall, the boundary condition for the chemical potential μ is simply the no-flux condition,

$$\boldsymbol{n}_w \cdot \nabla\mu|_S = \frac{\partial \mu}{\partial n_w}\bigg|_S = 0, \tag{7}$$

where $\boldsymbol{n}_w$ denotes the unit normal vector on the wall pointing *into* the fluid. For the order parameter ϕ, there are different kinds of boundary conditions in the literature with varying degree of complexity.[38–45] Huang, Huang, and Wang[46] compared several types of boundary conditions for the study of drop dewetting. Here the WBC in geometric formulation proposed by Ding and Spelt[41] is adopted because of its certain advantages. The geometrical WBC abandons the surface energy integral in Eq. (1) and starts from some geometric considerations. It assumes that the contours of the order parameter in the diffuse interface are parallel to each other, including in the region near the surface. Then, the unit vector normal to the interface, denoted by $\boldsymbol{n}_s$, may be written in terms of the gradient of the order parameter as[41]

$$\boldsymbol{n}_s = \frac{\nabla\phi}{|\nabla\phi|}. \tag{8}$$

By noting that the vector $\nabla\phi$ may be decomposed as

$$\nabla\phi = (\boldsymbol{n}_w \cdot \nabla\phi)\boldsymbol{n}_w + (\boldsymbol{t}_w \cdot \nabla\phi)\boldsymbol{t}_w, \tag{9}$$

where $\boldsymbol{t}_w$ is the unit tangential vector along the wall, one finds that the contact angle θ at the contact line may be expressed by

$$\tan\left(\frac{\pi}{2} - \theta\right) = \frac{-\boldsymbol{n}_w \cdot \nabla\phi}{|\nabla\phi - (\boldsymbol{n}_w \cdot \nabla\phi)\boldsymbol{n}_w|} = \frac{-\boldsymbol{n}_w \cdot \nabla\phi}{|(\boldsymbol{t}_w \cdot \nabla\phi)\boldsymbol{t}_w|}. \tag{10}$$

Thus, one has

$$\frac{\partial \phi}{\partial n_w}\bigg|_S = -\tan\left(\frac{\pi}{2} - \theta\right)|\boldsymbol{t}_w \cdot \nabla\phi|. \tag{11}$$

In the design of this geometric WBC, the following fact has been taken into account: the tangential component of ϕ's gradient cannot be modified during simulation and the local (microscopic) contact angle can only be enforced through the change of the normal component.[41] Owning to this, the geometric WBC performs better than other surface-energy-based boundary conditions in assuring that the local contact angle matches the specified one.

C. Contact angle hysteresis model

The above boundary conditions are applicable for ideally smooth surfaces with given contact angle. In reality, however, perfectly smooth surfaces are rarely encountered and the CAH can play an important role. There exist some investigations on the relation between the CAH and the underlying surface heterogeneities at small scales (e.g., see the work by Kusumaatmaja and Yeomans[47]). Here we do not intend to consider the CAH by directly including the surface heterogeneities; instead, we assume the surface is sufficiently smooth at a relatively large scale and employ a phenomenological CAH model for contact lines. Specifically, the method presented by Ding and Spelt[32] (in phase-field simulation) and also used by Wang, Huang, and Lu[34] (in LBM simulation) is employed. In this method, the effects of CAH are considered as follows:

$$\left.\begin{array}{lll} \theta = \theta_A & \text{if} & V_{cl} > 0 \\ \theta_R < \theta < \theta_A & \text{if} & V_{cl} = 0 \\ \theta = \theta_R & \text{if} & V_{cl} < 0 \end{array}\right\}, \tag{12}$$

where V_{cl} is the contact line velocity. The implementation details will be described next.

D. Governing equations for hydrodynamics and numerical method

In the above sections, the basics of phase-field model for binary fluids, the wetting boundary condition as well as the contact angle hysteresis model have been presented. In this section, the governing equations of the fluid flow and the methods for the numerical solutions of all equations are briefly introduced.

When the interfacial tension effects are modeled by the phase-field model, the governing equations of the incompressible flow of binary fluids with *uniform density* and *variable viscosity* may be written as

$$\nabla \cdot \boldsymbol{u} = 0, \tag{13}$$

$$\partial_t \boldsymbol{u} + (\boldsymbol{u} \cdot \nabla)\boldsymbol{u} = -\nabla S_p + \nabla \cdot [\nu(\phi)(\nabla \boldsymbol{u} + (\nabla \boldsymbol{u})^T)] - \phi \nabla \mu + \boldsymbol{G}, \tag{14}$$

where S_p is a term similar to the hydrodynamic pressure in single-phase incompressible flow,[37] $\boldsymbol{G}$ is a body force (which may be zero or a function of space and time), and $\nu(\phi)$ is the kinematic viscosity which is a function of the order parameter. In this work, the following function is adopted to interpolate the viscosity from the order parameter,

$$\nu(\phi) = \left[\frac{1+\phi}{2}\frac{1}{\nu_A} + \frac{1-\phi}{2}\frac{1}{\nu_B}\right]^{-1}, \tag{15}$$

where ν_A and ν_B are the kinematic viscosities of fluid A (represented by $\phi = 1$) and fluid B (represented by $\phi = -1$), respectively. As pointed out by Lee and Liu[48] and Zu and He,[49] who employed Eq. (15) or its equivalent form in LBM simulations of binary fluids, this form of function for $\nu(\phi)$ performs better than the commonly used linear function in phase-field simulations, which reads,[50,51]

$$\nu(\phi) = \frac{1+\phi}{2}\nu_A + \frac{1-\phi}{2}\nu_B. \tag{16}$$

We note that Coward *et al.*[52] analyzed the issue of viscosity interpolation and proposed the use of Eq. (15) much earlier in the volume-of-fluid simulation of two-phase flows.

The complete set of governing equations of binary fluids considered in this work consists of Eqs. (13), (14), and (6). The first two are solved by the lattice-Boltzmann method and the third is solved by the finite-difference method for spatial discretization and the 4th-order Runge-Kutta method for time marching. The whole method is called the hybrid lattice-Boltzmann finite-difference

method. The present formulation is simplified from another axisymmetric version presented by Huang *et al.*,[35] but with some extension for binary fluids with *variable viscosity*. Most of the details of this hybrid method can be found in Ref. [35]; for conciseness, they will not be fully repeated; here we mainly describe the extension for variable viscosity and the implementation of the geometric WBC with CAH model. It is noted that there are different choices for some of the components of the hybrid method in Ref. [35]. The present work uses the multiple-relaxation-time (MRT) collision model for LBM, the centered formulation (instead of the GZS formulation) for the forcing term, and the isotropic discretization based on the D2Q9 velocity model (i.e., the `iso` scheme in Ref. [35]) to evaluate the spatial gradients of the phase-field variables. The effects of variable viscosity are taken into account through the modification of one of the relaxation parameters in the MRT collision model, specifically the parameter τ_f,

$$\frac{1}{\tau_f(\phi) - 0.5} = \frac{1 + \phi}{2(\tau_{f,A} - 0.5)} + \frac{1 - \phi}{2(\tau_{f,B} - 0.5)}, \tag{17}$$

where $\tau_{f,A}$ and $\tau_{f,B}$ are two relaxation parameters related to the kinematic viscosities of fluids A and B (i.e., ν_A and ν_B) as

$$\nu_A = c_s^2(\tau_{f,A} - 0.5)\delta_t, \quad \nu_B = c_s^2(\tau_{f,B} - 0.5)\delta_t, \tag{18}$$

where $c_s = c/\sqrt{3}$ is the *lattice sound speed* in LBM (for the adopted D2Q9 velocity model), δ_t is the time step, and $c = \delta_x/\delta_t$ is the lattice velocity (δ_x, the grid size).

The spatial domain of simulation is a rectangle specified by $0 \le x \le L_x, 0 \le y \le L_y$, and this domain is discretized into $N_x \times N_y$ uniform squares of side length $h(=\delta_x)$, giving $L_x = N_x h$ and $L_y = N_y h$. The distribution functions in LBM and the discrete phase-field variables, $\phi_{i,j}$ and $\mu_{i,j}$, are both located at the centers of the squares (like the cell center in the finite-volume method). The indices (i, j) for the bulk region (i.e., within the computational domain) are $1 \le i \le N_x, 1 \le j \le N_y$. To facilitate the implementation of boundary conditions, a ghost layer is added on each side of the domain.

The WBC involves the enforcement of the normal gradient of the order parameter ϕ on the wall. Consider the case with the lower side being a wall with a given contact angle θ. The enforcement of ϕ's normal gradient is realized through a ghost layer of squares, the centers of which are $h/2$ below the wall with the index $j = 0$. When the geometric WBC is used, upon discretization of Eq. (11), one has

$$\phi_{i,0} = \phi_{i,1} + \tan\left(\frac{\pi}{2} - \theta\right)|t_w \cdot \nabla\phi|h. \tag{19}$$

Equation (19) contains the tangential component of ϕ's gradient on the wall $t_w \cdot \nabla\phi|_S$, and it is evaluated by the following extrapolation scheme,

$$t_w \cdot \nabla\phi|_S = 1.5 t_w \cdot \nabla\phi|_{i,1} - 0.5 t_w \cdot \nabla\phi|_{i,2}, \tag{20}$$

where the tangential gradients on the right-hand side are calculated by the central difference scheme, e.g.,

$$t_w \cdot \nabla\phi|_{i,1} = \left.\frac{\partial\phi}{\partial t_w}\right|_{i,1} = \frac{\phi_{i+1,1} - \phi_{i-1,1}}{2h}. \tag{21}$$

Once the order parameter in the ghost layer below the wall is specified according to Eq. (19), the normal gradient condition for ϕ is enforced. For a wall along some other directions, the formulas are similar (only some changes to the indices are required). It is noted that the above schemes for finite differencing and extrapolation are 2nd-order accurate.

The actual implementation of the CAH model given in Eq. (12) is as follows.[32] First, an initial approximation of the local contact angle on the wall, θ^{ia}, is obtained by using Eq. (10). Based on the range θ^{ia} belongs to (i.e., one of the three ranges divided by the advancing and receding angles, θ_A and θ_R), $\phi_{i,0}$ is specified in one of the following three manners (also take the lower side as an example):

- (1) if $\theta^{\text{ia}} \geq \theta_A$, set $\theta = \theta_A$ and then update $\phi_{i,0}$ by using Eq. (19);
- (2) if $\theta_R < \theta^{\text{ia}} < \theta_A$, keep $\phi_{i,0}$ unchanged;
- (3) if $\theta^{\text{ia}} \leq \theta_R$, set $\theta = \theta_R$ and then update $\phi_{i,0}$ by using Eq. (19).

We note that the present work only considers 2D problems and the implementation of the WBC with this CAH model is relatively easy as compared with the situation for 3D problems (which may be dealt with in future).

III. RESULTS AND DISCUSSIONS

A. Characteristic quantities, dimensionless numbers, and numerical parameters

Before showing the results, we introduce several important characteristic quantities and dimensionless numbers. In each of the problems below (including the validation cases and the WG-driven drop), a relevant length scale (for instance, the drop radius R or the channel height H (or some fraction of it, e.g., 0.25H)) is chosen to be the characteristic length L_c. Note that if the drop is only part of a circle, we take R as the radius of the *full* circle. The constant density is selected as the characteristic density ρ_c. The interfacial tension between the two fluids is σ. As given in Sec. II D, the kinematic viscosity of fluid A (making up the drop) is ν_A (its dynamic viscosity is $\eta_A = \rho_c \nu_A$) whereas that of fluid B (the ambient fluid) is ν_B (its dynamic viscosity is $\eta_B = \rho_c \nu_B$). The viscosity ratio is thus $r_\nu = \nu_A/\nu_B = r_\eta$. Based on the fluid properties, one can derive a characteristic velocity U_c,[53]

$$U_c = \frac{\sigma}{\rho_c \nu_A}. \tag{22}$$

Then, the characteristic time T_c is

$$T_c = \frac{L_c}{U_c} = \frac{L_c \rho_c \nu_A}{\sigma}. \tag{23}$$

The quantities of length, time, and velocity may be scaled by L_c, T_c, and U_c, respectively. In two-phase flows, the capillary number Ca and the Reynolds number Re are commonly used to characterize a problem. The capillary number Ca reflects the relative importance of the viscous force as compared with the interfacial tension force, and the Reynolds number Re reflects the ratio of the inertial force over the viscous force. With the above characteristic quantities, the capillary number is found to be

$$Ca = \frac{\rho_c \nu_A U_c}{\sigma} = 1, \tag{24}$$

and the Reynolds number is

$$Re = \frac{U_c L_c}{\nu_A} = \frac{\sigma}{\rho_c \nu_A} \frac{L_c}{\nu_A} = \frac{\sigma L_c}{\rho_c \nu_A^2}. \tag{25}$$

It is noted that the capillary number and the Reynolds number given in Eqs. (24) and (25) do not reflect the *actual* physics of the problem because the velocity scale U_c is purely derived from the physical properties of the fluid rather than taken as the characteristic dynamic velocities during the fluid motion. Nevertheless, they are helpful in setting up the simulation.

In addition, the Ohnesorge number Oh is also often used for drop dynamics.[54] It is defined as (note here the drop radius, instead of the diameter in Ref. 54, is used),

$$Oh = \frac{\rho_c \nu_A}{\sqrt{\rho_c \sigma R}}, \tag{26}$$

and it is related to the other dimensionless numbers as $Oh = 1/\sqrt{Re}$. No body force is included in the study of WG-driven drop, but in some validation cases a constant body force (per unit mass) g may be applied on the drop. For a drop of radius R under the action of a body force g, the Bond number may be defined as

$$Bo = \frac{\rho_c g R^2}{\sigma}, \tag{27}$$

which reflects the ratio of the body force over the interfacial tension force.

In phase-field-based simulations of two-phase flows, two additional parameters are introduced: (1) the Cahn number (the ratio of interface width over the characteristic length),

$$Cn = \frac{W}{L_c}, \tag{28}$$

and (2) the Peclet number (the ratio of convection over diffusion in the CHE),

$$Pe = \frac{U_c L_c^2}{M\sigma}. \tag{29}$$

There exist a few previous studies that investigated or discussed the issue on how to select Cn and Pe to get reliable results for various problems.[27,37] Since most of the problems studied in the present work have moving contact lines (MCLs), special attention is paid to the work by Yue, Zhou, and Feng,[27] who investigated the issue on how to attain the sharp interface limit (SIL) for problems involving MCLs and provided some useful guidelines. They found that the contact line dynamics is controlled by a diffusion length scale l_d with $l_d = \sqrt{M(\rho_c \nu)}$ when both fluids have the same viscosity, and in problems with a viscosity contrast, l_d is modified as $l_d = \sqrt{M(\rho_c \nu_e)}$ where $\nu_e = \sqrt{\nu_1 \nu_2} = \nu_1/\sqrt{r_\nu}$ is the effective viscosity (in Ref. 27 the dynamic viscosities were used; we consider two fluids with the same density, thus the kinematic viscosities can be used here). A dimensionless parameter $S = l_d/L_c$ (besides Pe) was introduced in Ref. 27 (note as we set $L_c = 1$, $S = l_d$, we may use S and l_d interchangeably below), and it was also found that the numerical results for a particular problem with MCLs approach a SIL as the Cahn number goes to zero with a fixed S; in other words, S should be scaled with Cn as $S \propto Cn^0$ in order to achieve the SIL (see Fig. 5 in Ref. 27). Besides, they suggested a criterion to achieve the SIL: $Cn_\epsilon < 4S$ where Cn_ϵ is the Cahn number based on their definition (the present Cahn number $Cn = 2\sqrt{2}Cn_\varepsilon$). We would like to also mention another important finding by Yue, Zhou, and Feng[27] that the slip length l_s is (approximately) related to the diffusion length l_d as $l_s = 2.5 l_d$. Thus the parameter S is related to the dimensionless slip length $\epsilon = l_s/L_c$ as $\epsilon = 2.5S$. Therefore, to change S (e.g., through the mobility) actually changes a physical parameter in problems with MCLs. The present definition of the Peclet number $Pe = (U_c L_c^2)/(M\sigma)$ differs from that by some others. Yue, Zhou, and Feng[27] defined the Peclet number as $Pe_1 = (U_c L_c W)/(2\sqrt{2}M\sigma)$ whereas the Peclet number defined by Villanueva and Amberg[55] and by Khatavkar, Anderson, and Meijer[53] is $Pe_2 = (U_c L_c W)/(3M\sigma)$. They are related to the present one as $Pe_1 = PeCn/(2\sqrt{2})$ and $Pe_2 = PeCn/3$, respectively. It is noted that the parameter S may be written as

$$S = \frac{1}{\sqrt{Pe\sqrt{r_\nu}}} = \frac{\sqrt{Cn}}{\sqrt{3Pe_2\sqrt{r_\nu}}}, \tag{30}$$

which shows that S is independent of the Cahn number Cn using the present definition of the Peclet number (but it becomes a function of Cn if the Peclet number defined in other works are used). In this work, some investigations about the Cahn number will also be carried out. Although the Peclet number is not a major focus, some discussions about its selection will be also given later.

The simulations are performed in the range $0 \leq t \leq t_e$, where t_e denotes the time at the end of the simulation. Suppose the characteristic length L_c is discretized by N_L uniform segments and the characteristic time T_c is discretized by N_t uniform segments, then one has

$$\delta_x = \frac{L_c}{N_L} \left(= \frac{L_x}{N_x} = \frac{L_y}{N_y} = h \right), \quad \delta_t = \frac{T_c}{N_t}. \tag{31}$$

B. Validation

As mentioned in Sec. I, the present numerical method is a simplified version (from axisymmetric to 2D geometry) of that given in Ref. 35. The hybrid method has been validated through the study of several drop problems in that work. Here three more validation tests are performed to check

the major extensions in the present work, including (1) the extension to handle binary fluids with different viscosities; (2) the capability to simulate drops on substrates with WG; (3) the CAH model.

1. Layered Poiseuille flow

In this test, the layered two-phase flow inside an infinitely long horizontal channel is considered. The channel height is $H = 2b$ and the x-axis is located at the center of the channel. The middle part ($-a \leq y < a$ where $0 < a < b$) is filled with one of the fluids (denoted as fluid 1) and the remaining regions ($-b \leq y < -a$ and $a \leq y \leq b$) are filled with the other fluid (denoted as fluid 2). Due to the symmetry about the x-axis, only the upper half ($0 \leq y \leq b$) is considered. The flow is driven by constant body forces in the horizontal direction with different magnitudes g_1 and g_2 acting on the inner and outer fluids, respectively. The two fluids have the same density and their kinematic viscosities are ν_1 and ν_2. This problem is essentially 1D with variations only in the vertical direction. In simulation, along the horizontal direction (with no variations) only four grid points were used and periodic boundary conditions were applied. The upper side is a stationary solid wall and the lower side is a symmetric line. Figure 1 illustrates the setup of the problem. Initially, the velocities were zero everywhere. Under the action of the body forces, a steady velocity profile is gradually developed. Upon reaching steady state, the velocity profile $u(y)$ may be found by analytical means,[56]

$$u(y) = \begin{cases} A_1 y^2 + C_1 & 0 \leq y < a \\ A_2 y^2 + B_2 y + C_2 & a \leq y \leq b \end{cases}, \tag{32}$$

where the coefficients are given by

$$A_1 = -\frac{g_1}{2\nu_1}, \quad A_2 = -\frac{g_2}{2\nu_2}, \quad B_2 = \left(-2A_2 + 2\frac{\nu_1}{\nu_2}A_1\right)a,$$

$$C_1 = (A_2 - A_1)a^2 - B_2(b-a) - A_2 b^2, \quad C_2 = -A_2 b^2 - B_2 b. \tag{33}$$

The parameter a is taken as $a = b/2 = H/4$ and is also chosen as the characteristic length, i.e., $L_c = a$. Four cases with different force magnitudes and distributions at different viscosity ratios were studied: (a) $g_1 = 1.46 \times 10^{-8}, g_2 = 0, \nu_1/\nu_2 = 0.1$; (b) $g_1 = 0, g_2 = 1.46 \times 10^{-8}, \nu_1/\nu_2 = 10$; (c) $g_1 = 0, g_2 = 1.46 \times 10^{-6}, \nu_1/\nu_2 = 0.1$; (d) $g_1 = 1.46 \times 10^{-6}, g_2 = 0, \nu_1/\nu_2 = 10$. The magnitudes of the body force are given in lattice units. The Reynolds numbers as defined in Eq. (25) are 1000, 1000, 100, and 100 for case (a), (b), (c), and (d), respectively (note that we always applied the non-zero body force on fluid A, which may be located either on the inner side (fluid 1) or the outer sider (fluid 2)). Figure 2 compares the velocity profiles obtained from the present simulations and those given by Eq. (32) for the above four cases. Note that the numerical solutions were obtained after the whole velocity field became steady and the velocities in Fig. 2 were scaled by the coefficient: max $(g_1/\nu_1, g_2/\nu_2)a^2$. From Fig. 2 it is observed that the numerical results agree quite well with the theoretical solutions for all the cases.
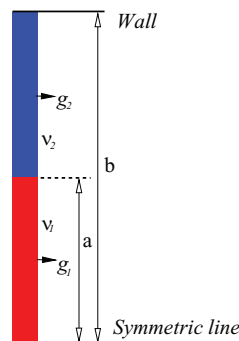
FIG. 1. Problem setup for the layered Poiseuille flow inside a channel.
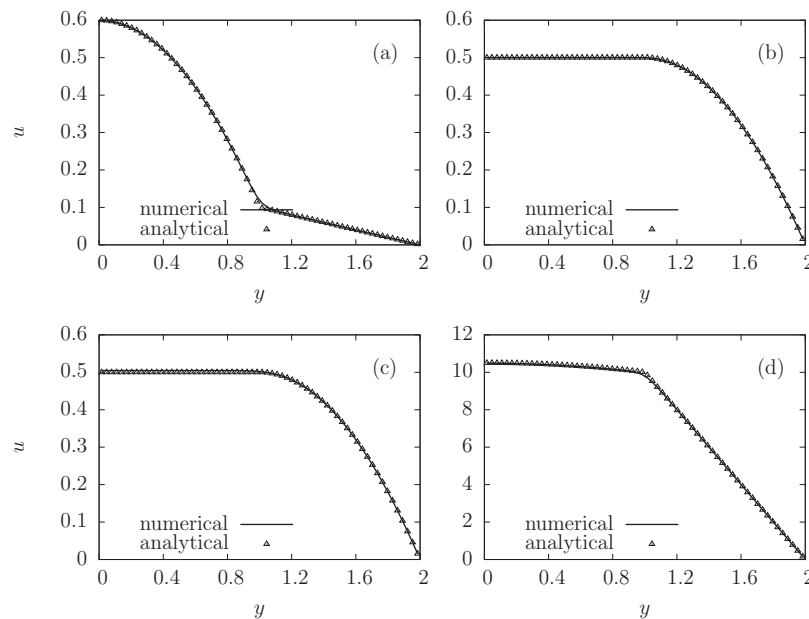
FIG. 2. Comparison of the velocity profiles of layered Poiseuille flow with analytical solutions given in Eq. (32) under four different conditions: (a) $g_1 = 1.46 \times 10^{-8}, g_2 = 0, \nu_1/\nu_2 = 0.1$; (b) $g_1 = 0, g_2 = 1.46 \times 10^{-8}, \nu_1/\nu_2 = 10$; (c) $g_1 = 0, g_2 = 1.46 \times 10^{-6}, \nu_1/\nu_2 = 0.1$; (d) $g_1 = 1.46 \times 10^{-6}, g_2 = 0, \nu_1/\nu_2 = 10$. The parameters are $Cn = 0.125, Pe = 5 \times 10^3, N_L = 32, N_t = 128$.

2. Liquid column in a channel with given WG

In the second test, a liquid column confined between two vertical flat plates located at $x = 0$ and $x = H$ is considered. The problem is symmetric about the middle vertical line $x = 0.5H$, thus only the left half ($0 \leq x \leq 0.5H$) is used in simulation. The characteristic length is chosen to be $L_c = H$. The problem setup is illustrated in Fig. 3. Initially, the liquid column has a (nominal) width of $W_{lc} = 4H$ (the distance between the two three-phase points (TPPs) in the vertical direction) and the y-coordinate of the middle point between the two TPPs is $y^{mid} = 3.5H$, giving the y-coordinates of the upper and lower TPPs: $y^{low} = 1.5H$ and $y^{upp} = 5.5H$. In the region with $y > y^{mid}$ the wettability of the plate is specified by a contact angle (CA) θ^{upp}, and for $y \leq y^{mid}$ the CA is θ^{low}, which is kept to be larger than θ^{upp}. The initial upper and lower interface shapes were specified according to θ^{upp} and θ^{low}. Both the upper and lower parts of the plate are assumed to be smooth (i.e., having no CAH). Because of the difference in the CAs, the liquid column is driven by the interfacial tension forces to move upwards (i.e., towards the more hydrophilic part).

To make sure that the liquid column is always under the action of the WG, $y^{mid} = (y^{low} + y^{upp})/2$ is updated at each step and the wettability distribution is updated based on y^{mid} to maintain the WG. After some time, the liquid column gradually reaches a steady state, which indicates a balance between the (driving) interfacial tension forces and the hydrodynamic resistances. It is noted that a similar problem was investigated by Esmaili, Moosavi, and Mazloomi,[14] who provided an approximate analytical solution for the development of the centroid velocity of the liquid column
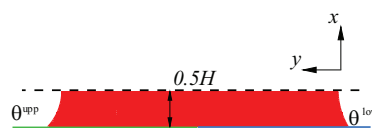
FIG. 3. Problem setup for a liquid column inside a channel with a stepwise WG (the figure is rotated by 90° in the anti-clockwise direction).
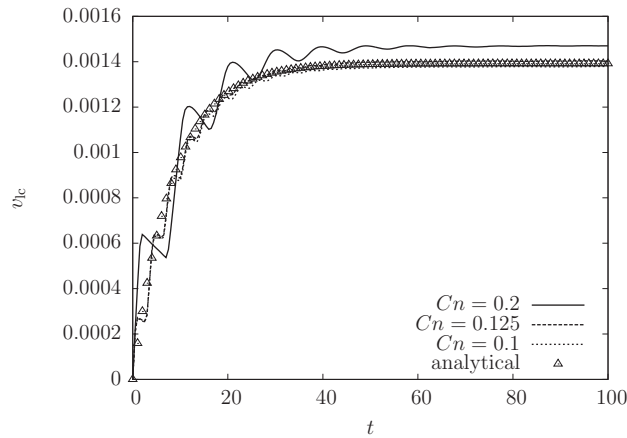
FIG. 4. Comparison of the evolutions of the centroid velocity of the liquid column v_{lc} driven by a stepwise WG obtained at three Cahn numbers ($Cn = 0.2, 0.125,$ and 0.1) with that predicted by Eq. (34). The other common parameters are $L_x = 0.5$, $L_y = 20$, $Re = 100$, $r_v = 1$, $\theta^{upp} = 47°$, $\theta^{low} = 59°$, $Pe = 5 \times 10^3$ ($S = 1.414 \times 10^{-2}$).

v_{lc} as

$$v_{lc} = \frac{\sigma H[2(\cos\theta^{upp} - \cos\theta^{low})]}{12\rho_c[\nu_A W_{lc} + \nu_B(L_y - W_{lc})]}(1 - e^{-t/t_s}), \tag{34}$$

where $t_s = H^2 L_y/[12(\nu_A W_{lc} + \nu_B(L_y - W_{lc}))]$. Corresponding to the above settings, boundary conditions for a stationary wall are applied on the left ($x = 0$) and on the right ($x = 0.5H$) symmetric boundary conditions are used. Periodic boundaries are assumed on the upper and lower sides of the simulation domain.

For this problem, three Cahn numbers were tried, including $Cn = 0.2, 0.125,$ and 0.1. The discretization parameter N_L takes 20, 32, and 40 for these Cahn numbers, respectively, so that the interface width (measured in the grid size h) is always 4.0. The common parameters are $L_x = 0.5$, $L_y = 20$, $Re = 100$, $r_v = 1$, $\theta^{upp} = 47°$, $\theta^{low} = 59°$, $Pe = 5 \times 10^3$ ($S = 1.414 \times 10^{-2}$). Figure 4 shows the evolutions of the centroid velocity of the liquid column v_{lc} obtained at the above three Cahn numbers for $0 \leq t \leq 100$. The centroid velocity v_{lc} was calculated as

$$v_{lc}(t) = \frac{\iint v(x, y, t)N(\phi)dxdy}{\iint N(\phi)dxdy} \approx \frac{\sum_{i,j} v_{i,j}(t)N(\phi_{i,j})}{\sum_{i,j} N(\phi_{i,j})}, \tag{35}$$

where the function $N(\phi)$ is given by

$$N(\phi) = \begin{cases} 1 & (\phi > 0) \\ 0 & (\phi \leq 0) \end{cases}. \tag{36}$$

Note that for this problem the characteristic length is taken as the channel height H. It is seen from Fig. 4 that at $Cn = 0.2$ the velocity shows relatively large fluctuations initially and then gradually approaches a constant value, which is slightly larger than the steady velocity predicted by Eq. (34). When Cn was reduced to 0.125, the amplitude of the fluctuation became much reduced and the velocity evolution obtained numerically became much closer to that by Eq. (34). To further reduce Cn to 0.1 only changed the results slightly. Based on the studies about a drop driven by WG (the main problem to be discussed later), the initial fluctuations appeared very likely because the initial state for the order parameter field was not sufficiently relaxed (details will be given below). Although the main problem differs from this one, it is suspected that the fluctuations have the same origin based on the common characteristic that they are reduced as the Cahn number decreases. In the study of the main problem, similar initial fluctuations in velocity were also observed though they were not as significant as in Fig. 4.
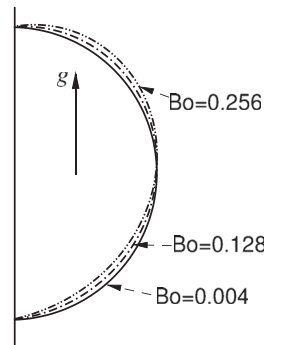
FIG. 5. Drop shape (in equilibrium) on a wall with CAH under the action of a body force at three different Bond numbers: $Bo = 0.004, 0.128, 0.256$.

3. Drop subject to a body force

In the third test, we consider a drop attached to a solid wall subject to a body force. When there is CAH on the wall, the drop may stay attached to the wall even under the action of the body force. This depends on the magnitude and direction of the body force, as well as the magnitude of the hysteresis effect (more specifically, on the advancing and receding angles, θ_A and θ_R, on the wall). In this problem, we assume that initially the drop is a semi-circle on the left wall with the center (of the circle) being $(x_c, y_c) = (0, 1.5)$. This shape corresponds to an initial contact angle of $\theta^i = 90°$. The body force acts along the y-direction on the drop only and its density (per unit mass) is g. The magnitude of the body force g was varied by changing the Bond number. The simulations were performed in a rectangular box with $L_x = 2$ and $L_y = 4$. Stationary wall was assumed on all boundaries and the left wall has CAH with $\theta_A = 105°$ and $\theta_R = 75°$. The common physical parameters are $Re = 16$, $r_\nu = 1$, and the numerical parameters are $Cn = 0.125$, $Pe = 5 \times 10^3$, $N_L = 32$, $N_t = 160$. Seven Bo numbers ($Bo = 2^{n+1} \times 10^{-3}$ with $n = 1, 2, \cdots, 7$) were tried. For this test we are mainly interested in the force balance when the drop is static. For all the Bo numbers considered, the drop finally reached a (nearly) static state. Under the action of the body force the drop deformed slightly and its centroid moved upwards a little bit, but the two TPPs were pinned due to the presence of CAH.

Figure 5 shows the shapes of the drop at three selected Bond numbers ($Bo = 0.004, 0.128, 0.256$) after the interfacial tension force balanced the body force and the drop reached static equilibrium. The increasing drop deformation with larger Bond number is well captured, as seen in Fig. 5. Figure 6 compares the evolutions the local dynamic contact angles at the upper and lower TPPs of the drop, $\overline{\theta}_d^{\text{upp}}$ and $\overline{\theta}_d^{\text{low}}$. Note that the angles were averaged over the interfacial region spanning a few grid points. Although the contours of the order parameter in this region should ideally be parallel to each other, we found that this could be slightly violated in the presence of CAH. Through such
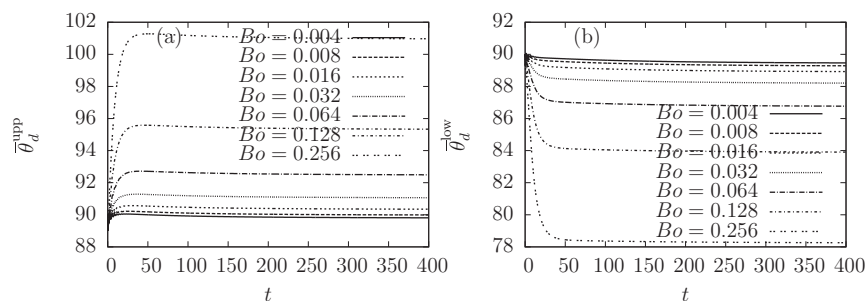
FIG. 6. Evolutions of the (averaged) dynamic contact angles at the upper and lower TPPs (on the wall) of the drop, $\overline{\theta}_d^{\text{upp}}$ and $\overline{\theta}_d^{\text{low}}$, under the action of a body force at seven Bo numbers: $Bo = 2^{n+1} \times 10^{-3}$ with $n = 1, 2, \cdots, 7$.
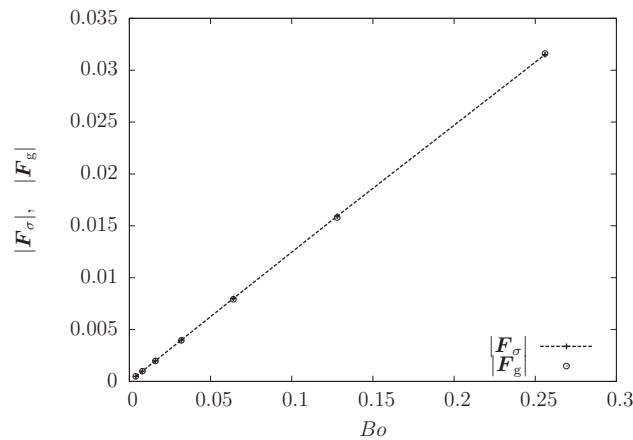
FIG. 7. Variations of the magnitudes of the net interfacial tension force $|\boldsymbol{F}_\sigma|$ (acting downwards) and the total body force $|\boldsymbol{F}_g|$ (acting upwards) on the drop (when in static equilibrium) with the Bond number.

an average, the accuracy of the interfacial force calculation becomes improved. It is observed from Fig. 6 that at the beginning $\overline{\theta}_d^{\mathrm{upp}}$ increases with time whereas $\overline{\theta}_d^{\mathrm{low}}$ decreases as time evolves. After the initial stage, the changes in both angles become quite small. At the same time, it is seen that for all of the Bo numbers $\overline{\theta}_d^{\mathrm{upp}}$ remains to be smaller than the advancing angle $\theta_A = 105°$ and $\overline{\theta}_d^{\mathrm{low}}$ is always larger than the receding angle $\theta_R = 75°$. The magnitude of the net interfacial tension force (per unit length) acting on the drop may be calculated as $|\boldsymbol{F}_\sigma| = \sigma(\cos\overline{\theta}_d^{\mathrm{low}} - \cos\overline{\theta}_d^{\mathrm{upp}})$ and this force pulls the drop downwards. The total body force $\boldsymbol{F}_g$ on the drop may be calculated by a simple integration over the area covered by the drop and it points upwards: $|\boldsymbol{F}_g| = \iint N(\phi)g\,dx\,dy = g\iint N(\phi)dx\,dy$ where the integral $\iint N(\phi)dx\,dy$ represents the area covered by the drop and the function $N(\phi)$ is given in Eq. (36). Figure 7 shows the variations of the magnitudes of these two forces on the drop (when in static equilibrium) with the Bo number. From Fig. 7, it is easy to see that the two kinds of forces has almost the same magnitudes for all the Bo numbers tested. This means that the balance condition for the drop was satisfied in the current simulations under all the Bo numbers.

4. Deformation of a drop on a wall with CAH subject to a shear flow

Another validation case is on the deformation of a drop on a wall with CAH in a shear flow. This case has been employed for validation of numerical methods involving the implementation of CAH for several times recently.[33, 34, 57] In the present work, we set up this problem as follows: in a box of size $L_x \times L_y$ a stationary drop is initially placed on the left wall (in the middle) with its shape corresponding to an initial contact angle $\theta^{\mathrm{i}} = 60°$. The right wall moves at a constant velocity U_w, thus creates a shear flow. The advancing and receding contact angles on the left wall are (θ_A, θ_R) $= (175°, 5°)$, so there is sufficient hysteresis to keep the drop pinned on the left wall. On the upper and lower sides, periodic boundary conditions are applied. Both fluids have the same density and viscosity. Two important parameters for this problem are:[57, 58] (1) the scaled drop area $A_d^* = 4A_d/L_x^2$ with $A_d = R^2(\theta^{\mathrm{i}} - \sin\theta^{\mathrm{i}}\cos\theta^{\mathrm{i}})$ being the area of the drop; (2) the capillary number based on the velocity near the top of the drop, $Ca_s = \rho\nu(h_d/L_x)U_w/\sigma$, with $h_d = R(1 - \cos\theta^{\mathrm{i}})$ being the initial height of the drop. For brevity, the problem setup is not shown here. We study this problem at three capillary numbers (by varying U_w) $Ca_s = 0.05, 0.1$, and 0.15 while keeping $A_d^* = 0.5$ (the domain size is $L_x \times L_y \approx 2.217 \times 8.867$). The Reynolds number is $Re = 0.4$, and other parameters are $Cn = 0.125$, $Pe = 5 \times 10^3$, $N_L = 32$, $N_t = 9600$. The deformed shapes of the drop (after the flow fully developed) under the three capillary numbers are plotted in Fig. 8 (also shown are the results by Schleizer and Bonnecaze[58] obtained using the boundary-integral method under the same parameters). It is seen from Fig. 8 that the present drop shapes agree well with those predicted by the boundary-integral method.
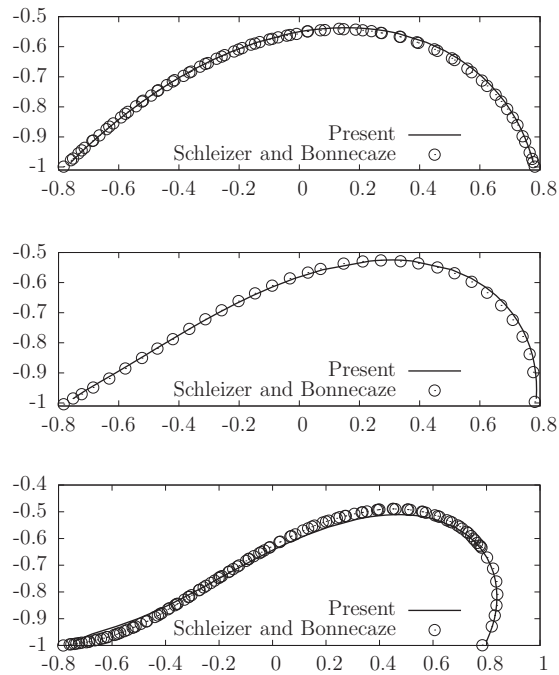
FIG. 8. Shape of a drop on a wall with contact angle hysteresis subject to a shear flow after sufficient development (the figure is rotated by 90° in the anti-clockwise direction). From top to bottom, the capillary numbers are $Ca_s = 0.05$, 0.1, and 0.15, respectively.

5. Motion of a flat drop on a wall with a stepwise WG

Besides, we have studied a relatively flat drop driven by a stepwise WG under a setting resembling one of the cases reported in Ref. 15. The initial setup is given in Fig. 9. This problem is actually similar to the main problem to be studied next except that the drop is quite flat and some other parameters differ. Several parameters are determined based on one case in Ref. 15 in which the immersion oil (with a surface tension $\sigma = 37.11$ mN/m and a dynamic viscosity $\eta = 98$ cP) was used, the advancing angle of the hydrophilic part was 23° and the receding angle of the hydrophobic part was 35.4°. The density of the immersion oil used in the experiment was not provided by Ondarcuhu and Veyssie,[15] and we use the value $\rho = 923$ kg/m^3 (at 23 °C)[59]. The width of the ridge varied from 1–3 mm in the experiments (comparable to the capillary length). Here we use a width of $L_{\text{drop}} = 1.5$ mm. The interface is initialized to be an arc of a circle with its center located at $(x_c, y_c) = (-\sqrt{3}R/2, R)$, which gives an initial contact angle of 30°. It is easy to find that $R = L_{\text{drop}} = 1.5$ mm. These parameters give a Reynolds number $Re = \rho U_c R/\eta = \rho \sigma R/\eta^2 \approx 5.35$. To reduce the effects of the ambient fluid, we use a large viscosity ratio $r_v = 50$. Because the drop is very flat (its volume occupies only a small fraction of the full circle of radius R), it is necessary to
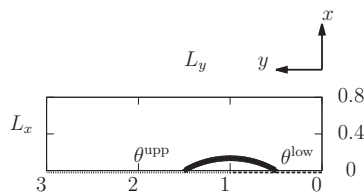
FIG. 9. Problem setup for a flat drop inside a box of size $L_x \times L_y = 0.8 \times 3$ with a stepwise WG on the left wall (the figure is rotated by 90° in the anti-clockwise direction). The radius of the circle is R and its initial origin is $(x_c, y_c) = (-\sqrt{3}R/2, L_y/3)$ (corresponding to an initial contact angle 30°). The contact angle of the left wall is $\theta^{\text{upp}} = 23°$ for $y > y_c$ and θ^{low} for $y < y_c$.

employ a small Cn number; otherwise, it will shrink significantly and even dissolve completely in the ambient fluid (see the part on the initial relaxation, Subsection III C 4, to be given later). Here we use $Cn = 0.025$ with the interface thickness in grid size $W/h = 4$ and a spatial discretization parameter $N_L = 160$ ($Cn_\epsilon \approx 8.8 \times 10^{-3}$). The Peclet number is $Pe = 5 \times 10^3$. Then, the parameter S is found to be $S \approx 5.32 \times 10^{-3}$ and the dimensionless slip length is $\epsilon = l_s/L_c = 2.5S \approx 1.33 \times 10^{-2}$ (i.e., the slip length is about $l_s \approx 20\ \mu$m). Note that we do not intend to simulate a drop *exactly* under the same condition as the experiment because of some difficulties and limitations of the present method. For instance, the density ratio is limited to be unity here (though for flows at small Reynolds numbers the density ratio is not a very important parameter); besides, as mentioned above, the slip length in a real system is usually very small (of molecular size) and it is extremely demanding (beyond our capability) to fully resolve it in numerical simulations. Although being already quite small, the slip length used for the simulation ($l_s \approx 20\ \mu$m) is still several orders of magnitude larger than the real slip length. What we actually do here is to compare the simulated results for the steady drop velocity with those predicted by an equation derived based on certain assumptions, which was also used by Ondarcuhu and Veyssie[15] for comparison with their experimental results. This equation predicts the steady capillary number as

$$Ca_{\text{drop}} = \frac{1}{6l}\sqrt{\frac{(\theta^{\text{low}})^2 + (\theta^{\text{upp}})^2}{2}}\left(\frac{(\theta^{\text{low}})^2 - (\theta^{\text{upp}})^2}{2}\right), \tag{37}$$

where all angles are in radian, and l is the constant prefactor mentioned above ($l = \ln(k_l L_c/l_s) = \ln(k_l/\epsilon)$). In the derivation of Eq. (37) a few assumptions were made.[5,15] For example, the pressure was assumed to reach equilibrium much faster than the drop's motion and the profile of the drop remains an arc of circle. And the drop was assumed to be quite flat with the contact angle being much smaller than unity (one radian). Besides, the resistance due to the ambient fluid was assumed to be negligible. Here we fix the contact angle on the upper part at $\theta^{\text{upp}} = 23°$ and try several lower contact angles: $\theta^{\text{low}} = 30°$, $33°$, $35.4°$, $38°$, and $40°$. The current settings should not cause large deviations from those assumptions for Eq. (37) and the major difference is mainly in the slip length. The centroid velocity of the drop v_{drop} was calculated as in Eq. (35). Under the action of the WG, the drop gradually reaches a steady state and the steady drop velocity is denoted by V_{drop}. The steady capillary number Ca_{drop} is defined based on V_{drop},

$$Ca_{\text{drop}} = \frac{\rho_c \nu_A V_{\text{drop}}}{\sigma}, \tag{38}$$

which just corresponds to the drop velocity V_{drop} measured in the characteristic velocity U_c. Figure 10 shows the variation of the steady capillary number Ca_{drop} with the lower contact angle θ^{low}. For comparison, the respective predictions of Ca_{drop} by Eq. (37) with $k_l = 0.152, l = 2.44$ and $k_l = 0.189, l = 2.65$ are also plotted in Fig 10. It is seen that with some suitable value of the
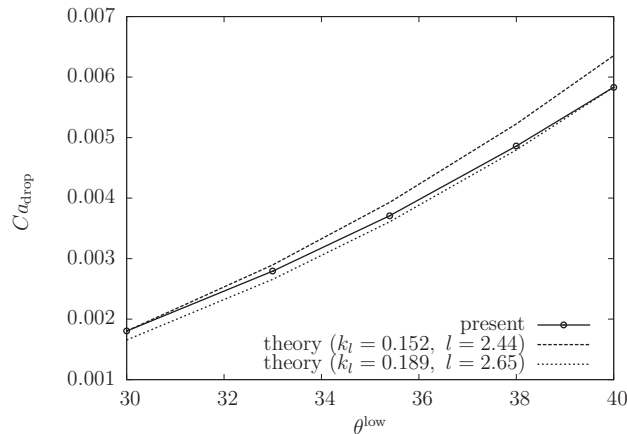
FIG. 10. Variation of the steady capillary number Ca_{drop} with the lower contact angle θ^{low} for a flat drop driven by a stepwise WG.
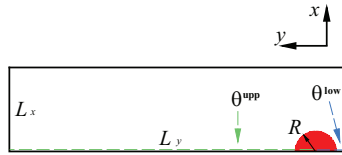
FIG. 11. Problem setup for a (semi-circular) drop inside a rectangular box with a stepwise WG. Note that the figure is rotated by 90° in the anti-clockwise direction. The radius of the circle is R and its initial origin is $(x_c, y_c) = (0, 1.5R)$. The domain size is $L_x \times L_y = 4R \times 16R$. The contact angle of the wall in touch with the drop is θ^{upp} for $y > y_c$ and θ^{low} for $y < y_c$.

constant k_l the numerical results can match Eq. (37) very well. Here, the suitable value of k_l seems to be of order $O(0.1)$. Another observation is that the prefactor l that gives the best agreement seems to increase slightly as the difference between the contact angles increases (for example, $l = 2.44$ for $(\theta^{\text{upp}}, \theta^{\text{low}}) = (23°, 30°)$, $\Delta \cos \theta = 0.0545$, and $l = 2.65$ for $(\theta^{\text{upp}}, \theta^{\text{low}}) = (23°, 40°)$, $\Delta \cos \theta = 0.1545$). It is interesting to note that similar trend was reported by Ondarcuhu and Veyssie[15] when they compared their experimental results with the theoretical ones: for $(\theta^{\text{upp}}, \theta^{\text{low}}) = (23°, 35.4°)$, $\Delta \cos \theta = 0.1054$, $l = 12.8$ gave the best fit, whereas for $(\theta^{\text{upp}}, \theta^{\text{low}}) = (19.2°, 38°)$, $\Delta \cos \theta = 0.1564$, $l = 13.5$ was the best.

C. Drop driven by WG

1. Problem setup

Now we study the main problem in this work, namely, a drop on a wall subject to a stepwise WG. Figure 11 illustrates the overall setup. There is no body force in this problem (i.e., it is assumed that the Bond number is negligibly small). This problem resembles that in Sec. III B 2 to some extent except that the domain is now a rectangular box with solid walls on all boundaries and the object under consideration is a drop in touch with one wall only. In addition, the wall in touch with the drop may have hysteresis effects. Therefore, in addition to the contact angles at the upper and lower parts, θ^{upp} and θ^{low}, four additional parameters may come into play in this problem. They are the advancing and receding angles of the upper and lower parts: $\theta_A^{\text{upp}}, \theta_R^{\text{upp}}, \theta_A^{\text{low}}, \theta_R^{\text{low}}$. In fact, for walls with CAH, it should suffice to just give the advancing and receding angles, θ_A and θ_R, instead of the contact angle θ, which may possibly take any value between θ_A and θ_R. However, here we still keep the usual contact angle because it represents the limiting case when the CAH approaches zero (i.e., $\theta_A \rightarrow \theta$ and $\theta_R \rightarrow \theta$). In this way, the CAH effect may be better appreciated. For convenience, when $\theta_H = \theta_A - \theta_R$ is not zero, we assume that $\theta = (\theta_A + \theta_R)/2$. Note that in Fig. 11 the drop has a *semi-circular* shape (with the origin of the circle located on the y-axis, i.e., $x_c = 0$). This initial shape corresponds to an initial contact angle $\theta^i = 90°$, and it is used below as the default setting.

2. Observables of interest

In this problem, we are mainly interested in the following observables: (1) the (instantaneous) average drop velocity (or the centroid velocity of the drop), $v_{\text{drop}}(t)$; (2) the dynamic contact angles (DCAs) *near* the upper and lower three-phase-points, $\theta_{d,\text{nw}}^{\text{upp}}(t)$, and $\theta_{d,\text{nw}}^{\text{low}}(t)$; (3) the (instantaneous) position and velocity of the contact line, $y_{\text{cl}}(t)$ and $v_{\text{cl}}(t)$. The two DCAs, $\theta_{d,\text{nw}}^{\text{upp}}$ and $\theta_{d,\text{nw}}^{\text{low}}$, were measured at the interface (where $\phi = 0$) along the layer next to the outermost one (i.e., along the line which is $1.5\delta_x$ away from the wall with WG). The contact line velocity $v_{\text{cl}}(t)$ is calculated by numerical differentiation of the contact line position $y_{\text{cl}}(t)$ as $v_{\text{cl}}(t) = (y_{\text{cl}}(t) - y_{\text{cl}}(t - \delta_t))/\delta_t$. When v_{cl} is scaled by the characteristic velocity U_c, it becomes the capillary number of the contact line, i.e., $Ca_{\text{cl}}(t) = v_{\text{cl}}(t)/U_c$. As the upper CL is advancing and the lower is receding, the corresponding capillary numbers are denoted by Ca_{acl} and Ca_{rcl}, respectively. In most cases studied here, the drop eventually reached a (nearly) steadily moving state. We will focus especially on the steady state, which in theory is reached only when $t_e \rightarrow \infty$ (if the drop is in an infinitely large domain). In practice, it is determined by the following criterion for the drop velocity $v_{\text{drop}}(t)$ (with $t \geq \Delta t$ where

$\Delta t = \sqrt{Re}\,T_c$),

$$\left| \frac{v_{\text{drop}}(t) - v_{\text{drop}}(t - \Delta t)}{v_{\text{drop}}(t)} \right| < 0.25\%. \tag{39}$$

That is, the relative change of v_{drop} in one Δt is less than 0.25%. The time to reach the steady state depends on various physical parameters: in many cases below, $t_e = 50\Delta t$ guarantees that Eq. (39) can be satisfied; for some cases (e.g., at very low Re), even longer time (e.g., $t_e = 300T_{c,\text{inv}}$) may be required. It is noted that at large viscosity ratio the velocity showed some fluctuations (which made it difficult to satisfy Eq. (39)) even though it seemed to have already entered a stable stage. In those cases, the simulations were terminated at certain time (say, $t_e = 50\Delta t$) when the fluctuations became reasonably small (e.g., the criterion is relaxed to 0.75%). The steady drop velocity V_{drop} is equivalent to V_{mig} defined by Xu and Qian[13] and it is no longer a function of time.

In Sec. III A, we defined the Reynolds number Re based on the characteristic velocity U_c (cf. Eq. (25)) rather than the *actual* drop velocity. To more realistically reflect the physics of the problem, one may define another Reynolds number based on V_{drop} as

$$Re_{\text{drop}} = \frac{V_{\text{drop}} R}{\nu_A}, \tag{40}$$

which is related to Re and Ca_{drop} as

$$Re_{\text{drop}} = \frac{V_{\text{drop}}}{U_c} Re = Re\, Ca_{\text{drop}}. \tag{41}$$

For a real problem, the Reynolds number Re may be calculated once the drop dimension and the fluid properties are specified. Since $Re_{\text{drop}} = Re\, Ca_{\text{drop}}$, we will mainly focus on Ca_{drop}. In general, Ca_{drop} may depend on the size of the domain to certain extent. For simplicity, we concentrate on the situation in which the drop stays in a confined space with the domain size being $L_x \times L_y = 4R \times 16R$ unless specified otherwise. Then, one may write Ca_{drop} as a function of all the remaining physical factors that appear in this problem,

$$Ca_{\text{drop}} = f(Re, r_\nu, \theta^{\text{upp}}, \theta_H^{\text{upp}}, \theta^{\text{low}}, \theta_H^{\text{low}}). \tag{42}$$

3. Parameter setting and the attainment of the sharp-interface limit

For numerical simulations, the results may depend on the spatial and temporal discretization parameters N_L and N_t as well (i.e., convergence in space and time). In addition, for phase-field-based simulations, the results depend to some extent on more factors including the Cahn number Cn and the Peclet number Pe (i.e., convergence towards the SIL).[27,37] We first briefly describe some parameters mostly used and then present some studies regarding the issue of convergence, which may justify our choices. Specifically, the spatial discretization parameter is fixed at $N_L = 32$ for most simulations unless specified otherwise (i.e., the radius of the drop is discretized into 32 uniform segments), the Cahn number is fixed at $Cn = 0.125$ which means that the interfacial width is about an eighth of the drop radius and spans about $N_L \times Cn = 4$ grid points, and the Peclet number is fixed at $Pe = 5 \times 10^3$. It is noted that the present definition of Cahn number differs from some others: if one adopts the definition used by Yue, Zhou, and Feng[27] and also by Ding, Spelt, and Shu[60] where the interface width ϵ is related to the present one as $\varepsilon = W/(2\sqrt{2})$, one would have an even smaller Cahn number of 0.044. In the computational domain, both the characteristic length $L_c = R$ and the characteristic time T_c are fixed to be unity (so is the characteristic velocity U_c). When the spatial discretization parameter is fixed at $N_L = 32$, in general it is not viable to use a fixed temporal discretization parameters N_t. From Eqs. (18) and (25), and also by noting that

$$c = \frac{\delta_x}{\delta_t} = \frac{L_c}{N_L} \frac{1}{T_c/N_t} = \frac{N_t}{N_L} U_c,$$

one can derive the following relations to determine the relaxation parameters $\tau_{f,A}$ and $\tau_{f,B}$,

$$\tau_{f,A} = 0.5 + \frac{3N_L^2}{ReN_t}, \quad \tau_{f,B} = 0.5 + \frac{3N_L^2}{r_v ReN_t}. \tag{43}$$

In LBM simulations, it is important to keep the relaxation parameter in an appropriate range to guarantee the stability and accuracy. Thus, we used different temporal discretization parameters N_t for different cases (depending on the Reynolds number and the viscosity ratio, as seen in Eq. (43)) to make sure that $0.5 < \tau_{f,A} < 2.0$ and $0.5 < \tau_{f,B} < 2.0$. The details about N_t for different cases will be given later.

In our work, the typical value of S is 1.414×10^{-2} and the Cahn number is $Cn = 0.125$ (giving $Cn_\epsilon = 0.04419$). Therefore, the condition $Cn_\epsilon < 4S$ can be satisfied. From Eq. (30) it is also obvious that $S \propto Pe^{-1/2}$ and $S \propto r_v^{-1/4}$. Thus, the condition to achieve the SIL for S, $S \propto Cn^0$, may be converted to that for Pe as $Pe \propto Cn^0$ (if one uses Pe_2, it is $Pe_2 \propto Cn$). Here we want to mention that for capillary-driven flows (e.g., drop spreading or the problem studied here) it is often not viable to know *in priori* the actual characteristic velocity (such as the steady drop velocity) that reflects the real characteristics of the problem before the simulation. The use of another velocity scale $\sigma/(\rho_c \nu)$ helps to define various parameters and set up the simulation. And based on our experience, it does not prevent us from achieving consistent sets of results (the same choice of U_c was adopted by Khatavkar, Anderson, and Meijer[53]). As discussed above and shown below, when Pe is defined as $Pe = (U_c L_c^2)/(M\sigma)$ (where $U_c = \sigma/(\rho_c \nu)$), for the present problem convergence towards a SIL can be observed with a fixed Pe and an increasingly smaller Cn ($Pe \propto Cn^0$ as $Cn \to 0^+$). To reduce the difference between the simulation and the SIL, the Cahn number should be as small as possible. We have tried even smaller Cahn numbers ($Cn = 0.0625$, and 0.03125) to investigate the convergence for one typical case with $Re = 16$, $r_v = 1$, $\theta^{\text{upp}} = 75°$, $\theta^{\text{low}} = 105°$, $\theta_H^{\text{upp}} = \theta_H^{\text{low}} = 0$, $L_x = 4$, $L_y = 16$. Figure 12 shows the evolutions of the instantaneous velocity of the drop v_{drop} under three Cahn numbers ($Cn = 0.125$, 0.0625, and 0.03125). Note that the computation for the smallest Cn ($Cn = 0.03125$ or $Cn_\epsilon = 0.011$) used $N_L = 128$ (the grid size being 512×2048) and $N_t = 10240$, thus it was much more time consuming. We terminated this computation at $t = 20$. Nevertheless, the results till $t = 20$ seem to be sufficient to show the convergence. It is seen from Fig. 12 that there are not quite significant changes in v_{drop} as Cn decreases. Some noticeable difference is observed in the initial acceleration stage between $Cn = 0.125$ and $Cn = 0.0625$ (see the inset in Fig. 12 for an enlarged view). However, the difference becomes very small when the velocity of the drop reaches the steady state. Besides, the two lines for $Cn = 0.0625$ and $Cn = 0.03125$ almost overlap with each other in Fig. 12. From these results, one can see a definite trend of convergence towards a SIL for the present problem for $Pe \propto Cn^0$ as $Cn \to 0^+$. It seems that to use $Cn = 0.125$ can provide fairly reliable
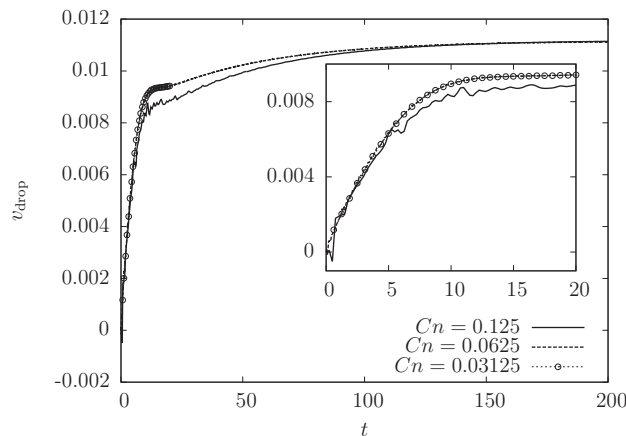
FIG. 12. Comparison of the evolutions of the drop velocity v_{drop} at three different Cahn numbers ($Cn = 0.125$, 0.0625, and 0.03125) with the Peclet number fixed at $Pe = 5 \times 10^3$ (or the parameter S fixed at $S = 1.414 \times 10^{-2}$). The other parameters are $Re = 16$, $r_v = 1$ $\theta^{\text{upp}} = 75°$, $\theta^{\text{low}} = 105°$, $\theta_H^{\text{upp}} = \theta_H^{\text{low}} = 0$, $L_x = 4$, $L_y = 16$.

predictions on the steady state of a drop driven by a stepwise WG (at least under the current settings). In addition, the interface shapes at the three Cahn numbers at a given time (even before the steady stage) were found to be very close: the difference between $Cn = 0.0625$ and $Cn = 0.03125$ could be barely seen and that between $Cn = 0.125$ and $Cn = 0.0625$ was quite small (for conciseness, the details are not given here). As noted above, the simulation becomes quite demanding when $Cn \to 0^+$, especially for simulations that use a uniform mesh. To keep the computational cost reasonable without incurring too large deviations from the SIL, we used $Cn = 0.125$ ($Cn_\epsilon = 0.04419$) in most cases; for some cases with a large viscosity ratio r_v (thus a small S as $S \propto r_v^{-1/4}$), $Cn = 0.0625$ ($Cn_\epsilon = 0.0221$) was used in order to satisfy the condition $Cn_\epsilon < 4S$.

4. On the initial relaxation of the order parameter field

For the above results, we used the following equation to initialize the order parameter field $\phi(x, y; 0)$,

$$\phi_{i,j}^0 = -\tanh\left(\frac{2(r_{i,j} - R)}{W}\right), \tag{44}$$

where $r_{i,j} = \sqrt{(x_{i,j} - x_c)^2 + (y_{i,j} - y_c)^2}$ is the distance between the cell center (x_i, y_j) and the drop center (x_c, y_c). Equation (44) gives the order parameter inside the drop as $\phi_{in} \approx 1$ and that outside the drop as $\phi_{out} \approx -1$. However, because of the curvature of the interface is finite (here, $1/R$), ± 1 are not the exact equilibrium values of ϕ far away from the interface. Even without any external deriving mechanisms (such as a WG, a body force or an external flow), the order parameter field would undergo a small change (mainly caused by the Cahn-Hilliard diffusion), making the order parameters inside and outside the drop become $\phi_{in}^{eq} = 1 + \epsilon_{in}$ and $\phi_{out}^{eq} = -(1 - \epsilon_{out})$ (ϵ_{in} and ϵ_{out} have some small positive values) and the radius of the drop decrease slightly to $R^{eq} = R + \delta r$ ($\delta r < 0$ and the magnitude of the relative change $|\delta r|/R$ is also small). Yue, Zhou, and Feng[61] studied this phenomenon systematically for a circular drop in a quiescent matrix and found that $\delta r/R$ is approximately given by

$$\frac{\delta r}{R} = -\frac{\sqrt{2}}{24}\left(\frac{V}{V_d}\right)\left(\frac{W/(2\sqrt{2})}{R}\right), \tag{45}$$

where V is the volume (area) of the computational domain, V_d is the volume (area) of the drop, and $W/(2\sqrt{2})$ corresponds to the interface thickness defined in their work. It seems that sufficient initial relaxation is required to obtain relatively smooth evolutions of some quantities of interest such as the drop velocity, especially when the Cahn number is not that small. For instance, some noticeable fluctuations can be seen in Fig. 12 during the initial acceleration stage at $Cn = 0.125$ (similar phenomenon is found in Fig. 4 as well). Without any relaxation before the simulation, the relaxation process occurs simultaneously with the main process that is studied (e.g., the flow caused by the WG). The two processes interfere with each other, leading to certain fluctuations. As will be found below, when a sufficiently relaxed order parameter field is employed for the initial condition (if possible to obtain such a relaxed field), the fluctuations are greatly reduced (even at a large viscosity ratio $r_v = 10$). Note that because of the shrinkage of the drop during the relaxation, the drop radius R_0 for the initial relaxation is set to be $R - \delta r$, which is slightly larger than R. For most cases of a drop driven by WG, the initial drop shape is semi-circular corresponding to an equilibrium contact angle of 90°. Thus, the drop volume is given by $V_d = \pi R^2/2$. Besides, the volume of the domain is $L_x \times L_y = 4R \times 16R = 64R^2$, and the Cahn number is $Cn = W/R = 0.125$. These parameters give $R_0 \approx 1.106R$. Probably because in this work the drop is attached to the wall (different from that studied by Yue, Zhou, and Feng[61]) and the estimate is rough, the drop does not shrink to have a radius of R exactly when we use $R_0 = 1.106R$. Some further adjustments and tests were carried out to obtain a relaxed initial field with the drop radius being very close to R (with $R_0 \approx 1.101R$, the deviation was less than 0.1%). Also note that during the initial relaxation, the contact angle is set to be 90° (i.e., no WG) to avoid any undesired flow (however, this requirement cannot be satisfied for the liquid column studied above in Sec. III B 2). Figure 13 shows the evolutions the drop velocity v_{drop} using two different initial conditions, one with initial relaxation for the order parameter field
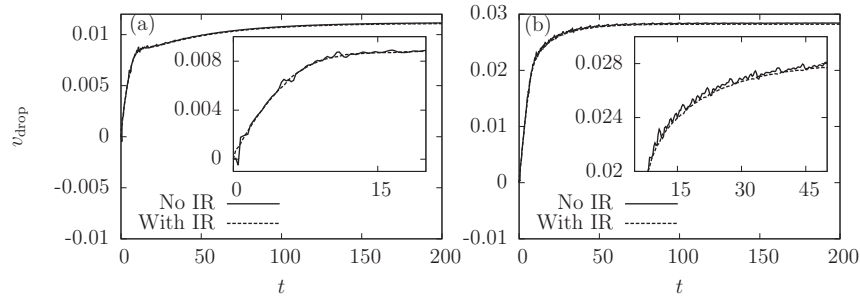
FIG. 13. Comparison of the evolutions of the drop velocity v_{drop} using different initial conditions for the order parameter field: (a) $r_v = 1$; (b) $r_v = 10$. The other parameters are $Re = 16$, $\theta^{\text{upp}} = 75°$, $\theta^{\text{low}} = 105°$, $\theta_H^{\text{upp}} = \theta_H^{\text{low}} = 0$, $L_x = 4$, $L_y = 16$, $Cn = 0.125$, $Pe = 5 \times 10^3$, $N_L = 32$, $N_t = 320$.

(IR) and the other without IR, for two typical cases with the viscosity ratio $r_v = 1$ and 10 respectively (the two insets in Fig. 13 enlarge the relevant segments with fluctuations for better view). It is seen that with IR the fluctuations and overshoots in v_{drop} can be hardly observed in Fig. 13 for both r_v = 1 and 10. Note that when one zooms in on the figure even further, some fluctuations of quite small magnitudes can be still observed for $r_v = 10$ (not quite visible in Fig. 13). We suspect that they might be related to the interpolation of the viscosity (relaxation parameter). As these remaining fluctuations are so small, we do not intend to dig into them here. Another observation is that the initial relaxation appears to have only quite small effects on the steady state. Detailed examinations on other quantities of interest give similar findings. Thus, we will not highlight whether a simulation is done with or without IR later when we are concerned about the steady state. In addition, as seen from Eq. (45), the change caused by IR is proportional to the Cahn number. Hence, for even smaller Cn the effects of IR will be more reduced, making the IR less significant to affect the simulation outcome (this has been confirmed by our numerical tests). Ideally, one should use a very small Cn, but that is too demanding for the simulation with uniform mesh. In our opinion, $Cn = 0.125$ (Cn_ϵ = 0.04419) seems to be already good enough.

5. Slip of the contact line

For the study of drop motion on a solid surface, one of the important issues is the slip of the contact line (CL). In Sec. II A, it was mentioned that in the present work the slip is generated by the diffusion in the Cahn-Hilliard equation (CHE). At the same time, there may be certain amount of slip generated by the LBM near the wall. We have investigated in detail the slip from the two mechanisms for a typical case in our simulation. In phase-field simulations, the motion of the interface is directly linked to the change of the order parameter ϕ. Therefore, to know the slip caused by the two mechanisms, we examined the change of ϕ on the wall per time step due to the convection and diffusion in the CHE: $(\Delta\phi)^{\text{conv}} = [-(\boldsymbol{u} \cdot \boldsymbol{\nabla})\phi]$ and $(\Delta\phi)^{\text{diff}} = [M\nabla^2\mu]$. It is noted that the quantities *on the wall* are obtained by using the linear extrapolation scheme (similar to Eq. (20)). Figure 14 compares the changes of the order parameter ϕ on the (left) wall caused by diffusion and convection in the CHE for a typical case when the drop reaches steady state. In Fig. 14, only a small portion of the boundary (of a length $4R$) that covers the two MCLs is shown, and the spatial coordinate is relative to the position of the lower MCL (receding CL, RCL) y_{rcl}. As expected, $(\Delta\phi)^{\text{diff}}$ and $(\Delta\phi)^{\text{conv}}$ are non-zero only near the two MCLs and vanish elsewhere. As found from Fig. 14, for typical cases in the present work, the slip is mainly caused by the diffusion in the CHE: the change of ϕ due to convection, $(\Delta\phi)^{\text{conv}}$, which is linked to the slip generated by LBM, is *less than a quarter* of ϕ's change due to Cahn-Hilliard diffusion, $(\Delta\phi)^{\text{diff}}$. Note that away from the interfacial regions where both $(\Delta\phi)^{\text{diff}}$ and $(\Delta\phi)^{\text{conv}}$ vanish, the ratio $(\Delta\phi)^{\text{conv}}/(\Delta\phi)^{\text{diff}}$ was set to zero (to avoid *division by zero*). Here we would like to mention that the use of linear extrapolation increases the gap between $(\Delta\phi)^{\text{diff}}$ and $(\Delta\phi)^{\text{conv}}$. We argue that the extrapolation makes the evaluation of the slip effects more accurate. Our experience shows that in LBM simulations of a Poiseuille flow (driven by a constant body force) that employ the half-way bounce-back scheme (as in this work), the velocities
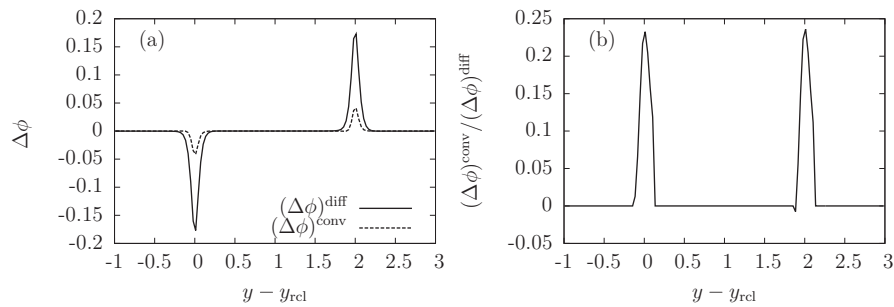
FIG. 14. Changes of the order parameter *on the wall* per time step due to diffusion and convection in the Cahn-Hilliard equation (CHE): (a) the absolute values of $(\Delta\phi)^{\text{diff}}$ and $(\Delta\phi)^{\text{conv}}$; (b) the ratio of the change due to convection over that due to diffusion $(\Delta\phi)^{\text{conv}}/(\Delta\phi)^{\text{diff}}$. The results are picked at $t = 200$ (steady state) from the case with $Re = 16$, $r_v = 1$, $\theta^{\text{upp}} = 75°$, $\theta^{\text{low}} = 105°$, $\theta_H^{\text{upp}} = \theta_H^{\text{low}} = 0$, $L_x = 4$, $L_y = 16$, $Cn = 0.125$, $Pe = 5 \times 10^3$ ($S = 1.414 \times 10^{-2}$), $N_L = 32$, $N_t = 320$.

on the wall obtained by extrapolation are (nearly) zero even when those in the first layer near the wall are finite and not negligible. It is expected that with the grid refined the slip caused by convection becomes even less significant. This has been confirmed by numerical tests. Figure 15 shows the ratio $(\Delta\phi)^{\text{conv}}/(\Delta\phi)^{\text{diff}}$ at the same moment ($t = 20$) for the same case simulated with different grid resolutions $N_L = 32$, 64, and 128 (at the same Peclet number). It is observed from Fig. 15 that with $N_L = 64$ the maximum of $(\Delta\phi)^{\text{conv}}$ becomes only about one tenth of that of $(\Delta\phi)^{\text{diff}}$, and with an even finer grid ($N_L = 128$), this ratio becomes about only 5% to 6%. Another note is that the slip due to diffusion is closely related to the mobility (or the Peclet number Pe). For the case selected for examination (which is typical in the present work), the Peclet number is $Pe = 5 \times 10^3$ and the Cahn number is $Cn = 0.125$, which correspond to $Pe_1 \approx 221$ or $Pe_2 \approx 208$. This value is comparable to those used by Khatavkar, Anderson, and Meijer[53] ($Pe_2 = 50$ and 500) where the characteristic velocity $U_c = \sigma/(\rho_c \nu)$ is the same as the present. It is noted that the restriction on the choice of mobility (Peclet number) due to the explicit RK4 may be alleviated to some extent by employing a small time step though this may increase the computation time significantly.

6. Some characteristics of the shape of the drop

The interface shape of the drop during its motion was carefully examined with a special focus on the extraction of the apparent contact angle. It was found that under a stepwise WG the interface
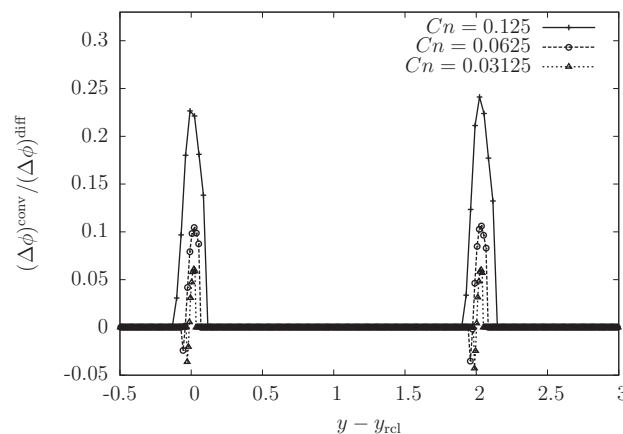
FIG. 15. The ratio of the change of the order parameter *on the wall* per time step due to convection over that due to diffusion in the CHE, $(\Delta\phi)^{\text{conv}}/(\Delta\phi)^{\text{diff}}$, at three Cahn numbers, $Cn = 0.125$, 0.0625, and 0.03125, with different grid resolutions $N_L = 32$, 64, and 128. The results are picked at $t = 20$ from the case with $Re = 16$, $r_v = 1$, $\theta^{\text{upp}} = 75°$, $\theta^{\text{low}} = 105°$, $\theta_H^{\text{upp}} = \theta_H^{\text{low}} = 0$, $L_x = 4$, $L_y = 16$, $Pe = 5 \times 10^3$ ($S = 1.414 \times 10^{-2}$).
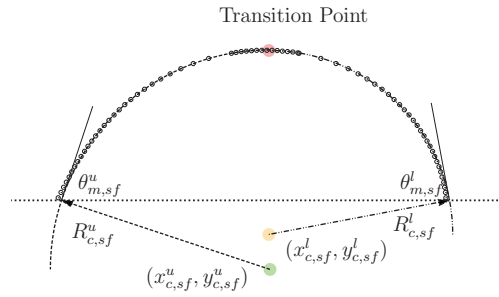
FIG. 16. Illustration of the shape fitting of the interface by two arcs connected at the top with different origins located at $(x_{c,sf}^u, y_{c,sf}^u)$ and $(x_{c,sf}^l, y_{c,sf}^l)$ and different radii R_{sf}^u and R_{sf}^l for the upper and lower portions, respectively. The dotted line represents the wall, the dashed line represents a quarter of the circle described by the equation $(x - x_{c,sf}^u)^2 + (y - y_{c,sf}^u)^2 = (R_{sf}^u)^2$, whereas the dash-dot-dotted line represents a quarter of the circle described by $(x - x_{c,sf}^l)^2 + (y - y_{c,sf}^l)^2 = (R_{sf}^l)^2$. The symbols are the interface points on the grid (i.e., intersection points between the contour $\phi = 0$ and the grid).

in steady state (with a relatively small velocity) may be divided into two portions with the transition point located at the top of the interface. Each portion (excluding the near-wall region) may be well fitted by a circle using the least-squares fitting technique. The two circles that fit the upper and lower parts have different origins and radii. For concreteness, they are denoted by $(x_{c,sf}^u, y_{c,sf}^u; R_{sf}^u)$ and $(x_{c,sf}^l, y_{c,sf}^l; R_{sf}^l)$, respectively. From these quantities, it is possible to derive the apparent contact angles of the two arcs, denoted by $\theta_{m,sf}^u$ and $\theta_{m,sf}^l$. Figure 16 illustrates the results of the above shape fitting and the extraction of the apparent contact angles based on the shape fitting for a case with $Re = 16$, $r_v = 1$, $\theta^{upp} = 60°$, $\theta^{low} = 90°$, $\theta_H^{upp} = \theta_H^{low} = 0$, $L_x = 4$, $L_y = 16$, $Cn = 0.125$, $Pe = 5 \times 10^3$ ($S = 1.414 \times 10^{-2}$), $N_L = 32$, $N_t = 320$. Besides, for each point on the interface (x_i, y_i) the deviation from the respective circle was also calculated and the maximum was monitored. It was found that during the simulation (excluding the early adjustment stage), the maximum deviation remained small (less than 1%; in most cases, less than 0.5%). Thus, the description of the interface through the above division into two segments seems to be well justified. In addition to the above way to find the apparent contact angle, there is another method recently proposed by Sui and Spelt[28] that may be used to extract the apparent contact angle. Sui and Spelt[28] found that the angle the interface makes with the wall is a function of the arclength from the contact line along the interface, $\theta = \theta(s)$. For viscous flow, $\theta(s)$ is (roughly) a linear function away from the wall. An apparent angle is obtained by extrapolating this function to the contact line ($s = 0$). Figure 17 shows the monitored $\theta(s)$ along the advancing and receding interfaces in (nearly) steady state and illustrates the above way to obtain another apparent contact angle. We also tried this method and the apparent angle obtained in this way is denoted as $\theta_{m,lf}$.

It is known that the flow around a moving contact line may be in general divided into three regions: the inner, intermediate, and the outer region.[23] Cox[23] studied the motion of the contact line in the viscous regime with both fluids being liquids and derived a formula between the contact line
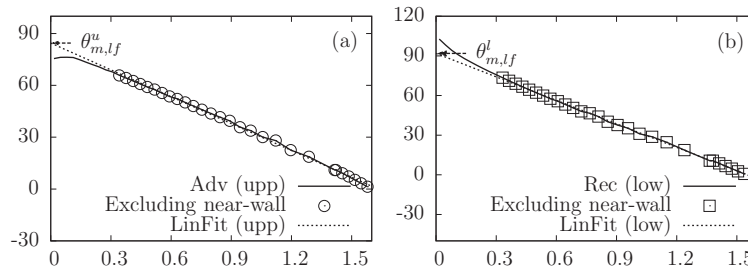
FIG. 17. Illustration of the way to obtain the apparent contact angle through extrapolating the function $\theta(s)$ to the contact line ($s = 0$).
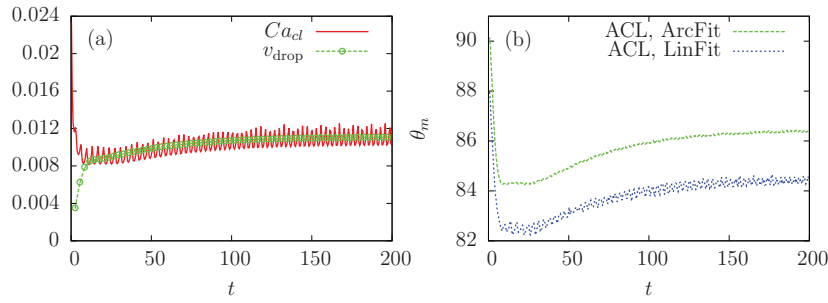
FIG. 18. Evolutions of (a) the capillary number Ca_{cl} based on the contact line velocity V_{cl} (b) the apparent contact angle θ_m (by arc-fitting and linear fitting) at the advancing contact line (ACL) on the upper part for the case with $Re = 16$, $r_v = 1$, $\theta^{upp} = 75°$, $\theta^{low} = 105°$, $\theta_H^{upp} = \theta_H^{low} = 0$, $L_x = 4$, $L_y = 16$, $Cn = 0.125$, $Pe = 5 \times 10^3$ ($S = 1.414 \times 10^{-2}$), $N_L = 32$, $N_t = 320$.

velocity V_{cl} (more precisely, the V_{cl}-based capillary number Ca_{cl}) and the apparent contact angle θ_m in the outer region. The zeroth-order value of θ_m may be expressed as[23]

$$g(\theta_m, \lambda) = g(\theta_w, \lambda) + Ca_{cl} \ln(\epsilon^{-1}), \qquad (46)$$

where θ_w is the (microscopic) contact angle on the wall, $\epsilon = l_s/L_c$ is the dimensionless slip length, λ is the ratio of the dynamic viscosities of the two fluids, and $g(\theta, \lambda) = \int_0^\theta [1/f(\beta, \lambda)]d\beta$ is a function of both the angle θ and the viscosity ratio λ ($\lambda = (\rho_c v_2)/(\rho_c v_1) = v_2/v_1 = 1/r_v$ in the present work) with the function $f(\beta, \lambda)$ given by

$$f(\beta, \lambda) = \frac{2 \sin \beta [\lambda^2 (\beta^2 - \sin^2 \beta) + 2\lambda\{\beta(\pi - \beta) + \sin^2 \beta\} + \{(\pi - \beta)^2 - \sin^2 \beta\}]}{\lambda(\beta^2 - \sin^2 \beta)\{(\pi - \beta) + \sin \beta \cos \beta\} + \{(\pi - \beta)^2 - \sin^2 \beta\}(\beta - \sin \beta \cos \beta)}. \qquad (47)$$

Note that the contact line velocity V_{cl} is positive for an advancing contact line (ACL) and negative for a receding contact line (RCL).[23] For simplicity, we always use a positive Ca_{cl} here, thus for a RCL the sign before Ca_{cl} in Eq. (46) is changed to the opposite. As noted before, one has $\epsilon = 2.5S$ and $S = 1/\sqrt{Pe\sqrt{r_v}}$ (see Eq. (30) above) in phase-field simulations.[27] We have investigated the relation between the apparent contact angle θ_m and the capillary number Ca_{cl} based on V_{cl} for various cases under different conditions and compared the present results with those predicted by Cox.[23] Figure 18 shows the evolutions of Ca_{cl} and θ_m at the ACL on the upper part (by arc-fitting and linear fitting, $\theta_{m,sf}^u$ and $\theta_{m,lf}^u$) for the case with $Re = 16$, $r_v = 1$, $\theta^{upp} = 75°$, $\theta^{low} = 105°$, $\theta_H^{upp} = \theta_H^{low} = 0$, $L_x = 4$, $L_y = 16$, $Cn = 0.125$, $Pe = 5 \times 10^3$ ($S = 1.414 \times 10^{-2}$), $N_L = 32$, $N_t = 320$. In Fig. 18(a) the instantaneous velocity of the drop v_{drop} is also plotted for reference. From Fig. 18(a) one can see that at the beginning Ca_{cl} is the largest (due to the abrupt enforcement of the contact angle) and it quickly decreases to oscillate near v_{drop}. In other words, after a short period the motions of the drop and the ACL are overall synchronized except that a small oscillation should be superimposed on the drop motion to obtain that of the ACL. From Fig. 18(b) it is found that the apparent contact angle obtained by the arc-fitting ($\theta_{m,sf}^u$) is slightly larger than that by linear-fitting ($\theta_{m,lf}^u$) (the maximum difference is about $2°$), and both show an initial overshoot in the early stage. It is also seen from Fig. 18(b) that $\theta_{m,sf}^u$ has smaller oscillations than $\theta_{m,lf}^u$, possibly because the least-squares fitting has better performance. Note that we had similar observations for the RCL (not shown here). Figure 19 shows the variations of the apparent contact angles with the capillary number Ca_{cl} based on the contact line velocity V_{cl} at the ACL on the upper part (left column) and at the RCL on the lower part (right column) for three cases with different parameters (see the figure caption for details). The small green and blue disks are used in Fig. 19 to circle the regions where the data of the pairs ($\theta_{m,sf}$, Ca_{cl}) and ($\theta_{m,lf}$, Ca_{cl}) are located when the drop enters the steady stage (note there are still small oscillations in these quantities at this stage, as seen in Fig. 18). The solid lines show the predictions by Cox.[23] It is noted that for the third row in Fig. 19 (the case with CAH), the contact angles on the wall (θ_w in Eq. (46)) take the values of the advancing and receding contact angles for the ACL and RCL, respectively. It is found from Fig. 19 that except during the early stage (when Ca_{cl} is quite
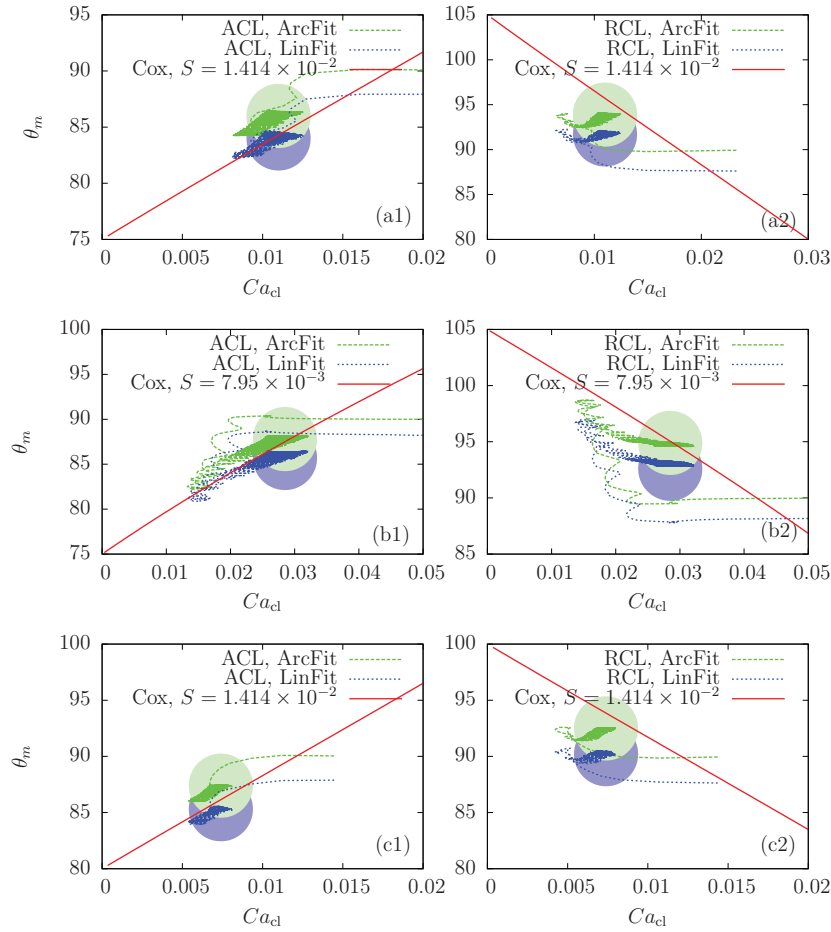
FIG. 19. Variation of the apparent contact angle θ_m with the capillary number Ca_{cl} based on the contact line velocity V_{cl} as the drop accelerates from the beginning, gradually reaches and remains in the steady state. The left column shows the advancing contact line (ACL) on the upper part, and the right shows the receding contact line (RCL) on the lower part. From top to bottom: (a) $r_v = 1$, $Cn = 0.125$, $Pe = 5 \times 10^3$ ($S = 1.414 \times 10^{-2}$), $\theta^{\mathrm{upp}} = 75°$, $\theta^{\mathrm{low}} = 105°$, $\theta_H^{\mathrm{upp}} = \theta_H^{\mathrm{low}} = 0$; (b) $r_v = 10$, $Cn = 0.0625$, $Pe = 5 \times 10^3$ ($S = 7.95 \times 10^{-3}$), $\theta^{\mathrm{upp}} = 75°$, $\theta^{\mathrm{low}} = 105°$, $\theta_H^{\mathrm{upp}} = \theta_H^{\mathrm{low}} = 0$; (c) $r_v = 1$, $Cn = 0.125$, $Pe = 5 \times 10^3$ ($S = 1.414 \times 10^{-2}$), $\theta^{\mathrm{upp}} = 75°$, $\theta^{\mathrm{low}} = 105°$, $\theta_H^{\mathrm{upp}} = \theta_H^{\mathrm{low}} = 10°$ (giving $\theta_A^{\mathrm{upp}} = 80°$ and $\theta_R^{\mathrm{low}} = 100°$). The common parameters are $Re = 16$, $L_x = 4$, $L_y = 16$.

large and the drop has not had enough time to adjust its shape) the relation between θ_m and Ca_{cl} generally follows the theoretical prediction (with the maximum deviation being just a few degrees). The best agreement is seen in the apparent contact angle by arc-fitting ($\theta_{m,\,sf}$) for the case with $r_v = 10$ and $Pe = 5 \times 10^3$ ($S = 7.95 \times 10^{-3}$) (the second row in Fig. 19) in which the data of ($\theta_{m,\,sf}$, Ca_{cl}) fall almost exactly on the theoretical line. The possible reason is that the slip length ($\epsilon = 2.5S$) is the smallest among all cases and that leads to better separation of different scales, which was assumed by Cox[23] in deriving the theoretical results. As the apparent contact angles may be calculated from the equations by Cox[23] once the capillary number Ca_{cl} (equal to Ca_{drop} in steady state) is known, we will mainly focus on the velocity of the drop in what follows. Some investigations on the dynamic contact angles near the wall will also be made in Sec. III C 7.

From Fig. 19, one can also find that the following relation holds for the (specified) contact angles on the wall (θ_w) and the apparent contact angles (θ_m) for the upper and lower parts: $\theta_w^{\mathrm{upp}} < \theta_m^u < \theta_m^l < \theta_w^{\mathrm{low}}$. In other words, the difference in the apparent contact angle between the upper and lower parts ($|\theta_m^u - \theta_m^l|$) is reduced as compared with that in the contact angle on the wall ($|\theta_w^{\mathrm{upp}} - \theta_w^{\mathrm{low}}|$). This reflects the effect of the drop motion on the shape of the drop. Besides, it is obvious that the difference in θ_m is nonzero, and the interface away from the wall cannot be fitted by a single arc.

This contradicts the assumption made in some theoretical work, e.g., by Brochard[5] (though it is noted that Brochard[5] considered a drop driven by a continuous WG of mild magnitude and the assumption may be approximately correct). At the same time, the present finding seems to agree with the experimental observation by Ondarcuhu and Veyssie,[15] who investigated a flat drop driven by a stepwise WG and always observed a difference between the contact angles on different patches. It should be noted that the contact angles measured in Ref. 15 may differ (by definition) from θ_m defined here. Nevertheless, the difference in either θ_m or the contact angle measured by Ondarcuhu and Veyssie[15] shows that the drop deforms from the shape of one single arc.

7. Effects of the Reynolds number and viscosity ratio

In this part, the effects of the Reynolds number Re and the viscosity ratio r_v are investigated while the other factors in Eq. (42) are fixed at $\theta^{\text{upp}} = 75°$, $\theta^{\text{low}} = 105°$, $\theta_H^{\text{upp}} = \theta_H^{\text{low}} = 0$ (i.e., there is no CAH).

First, we vary the Reynolds number while keeping the viscosity ratio at $r_v = 1$. Six Reynolds numbers spanning a wide range were considered, including $Re = 0.09, 1, 4, 16, 100$, and 400. The temporal discretization parameter N_t was varied for different Re: $N_t = 320, 640, 3200$, and 25600 for $Re \geq 16$, $Re = 4$, $Re = 1$, and $Re = 0.09$, respectively. The simulation time t_e was varied for different Re to make sure the steady state was reached. Figure 20 shows the evolutions of the drop velocity v_{drop} at five different Reynolds numbers: $Re = 0.09, 1, 4, 16$, and 400. Note that "LD" in this figure means the simulation was done with a "Larger Domain" of $L_x \times L_y = 8 \times 20$. As found from Fig. 20, the drop velocity v_{drop} increases with time under the action of the WG and gradually reaches a steady state at all Reynolds numbers and the values of the steady velocity V_{drop} (here equivalent to the steady capillary number Ca_{drop} because V_{drop} is measured in U_c) at different Re are quite close to each other. At $Re = 400$, V_{drop} appears to be smaller than others; however, when the domain size is increased to $L_x \times L_y = 8 \times 20$ it becomes close to others as observed in Fig. 20 (this suggests that at higher Re the simulation is more affected by the domain size). Thus, excluding the effects of domain size, one may expect from Fig. 20 that the steady capillary number of the drop driven by a stepwise WG is independent of the Reynolds number. The present results indicate that the capillary number of the drop is independent of the drop size, which seems to differ from that by Daniel *et al.*,[22] where it was predicted that (cf. Eq. (1) in that article),

$$Ca = \alpha R \frac{d(\cos\theta)}{dx}, \tag{48}$$

with x being the coordinate in the WG direction and α being a constant. This is because Daniel *et al.*[22] considered a continuously varying WG with the contact angle θ having a distribution that satisfies $d(\cos\theta)/dx = const$ whereas the present work considers a stepwise WG that is independent of the drop radius R. On the other hand, from Eq. (48) one may deduce that Ca is proportional to the change in $\cos\theta$ across the footprint of the drop. For convenience, we denote this quantity as $\Delta\cos\theta$. In the
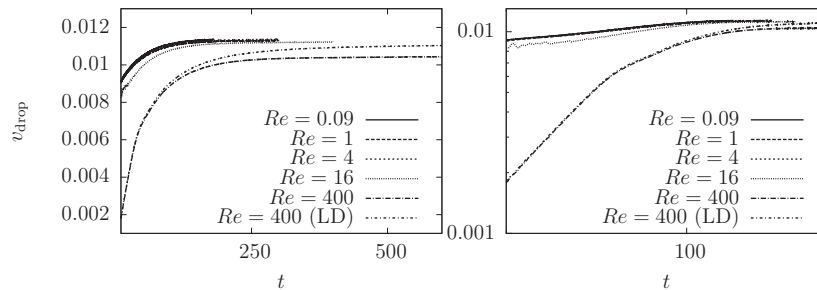
FIG. 20. Evolutions of the centroid velocity of the drop v_{drop} subject to a WG on a wall at different Reynolds numbers: $Re = 0.09, 1, 4, 16$, and 400. The common parameters are $r_v = 1$, $\theta^{\text{upp}} = 75°$, $\theta^{\text{low}} = 105°$, $\theta_H^{\text{upp}} = \theta_H^{\text{low}} = 0$, $L_x = 4$, $L_y = 16$, $Cn = 0.125$, $Pe = 5 \times 10^3$ ($S = 1.414 \times 10^{-2}$), $N_L = 32$. In the left panel both axes are in normal scale whereas in the right both are in logarithmic scale. The range for time is $10 \leq t \leq 600$.
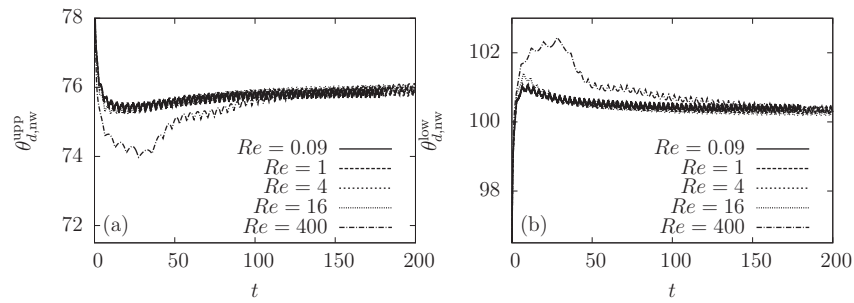
FIG. 21. (a, b) Evolutions of the dynamic contact angles near the upper (a) and lower (b) TPPs (measured at the next-to-outermost layer), $\theta_{d,\text{nw}}^{\text{upp}}$ and $\theta_{d,\text{nw}}^{\text{low}}$, of the drop subject to a stepwise WG at different Reynolds numbers: $Re = 0.09, 1, 4, 16,$ and 400. The common parameters are $r_\nu = 1$, $\theta^{\text{upp}} = 75°$, $\theta^{\text{low}} = 105°$, $\theta_H^{\text{upp}} = \theta_H^{\text{low}} = 0$, $L_x = 4$, $L_y = 16$, $Cn = 0.125$, $Pe = 5 \times 10^3$ ($S = 1.414 \times 10^{-2}$), $N_L = 32$.

case of a stepwise WG as in the present work, it may be expressed as $\Delta \cos \theta = \cos \theta^{\text{upp}} - \cos \theta^{\text{low}}$ and its effects will be studied in Sec. III C 8. At the same time, we would highlight that the present finding is favoured by the experimental study on a drop driven by a stepwise WG performed by Ondarcuhu and Veyssie,[15] who reported that the steady capillary number of the drop is indeed independent of the drop size (as long as it is small enough for the gravity effects to be neglected).

Figure 21 compares the evolutions of the DCAs near the upper and lower (Figs. 21(a) and 21(b)) TPPs at these Reynolds numbers: $Re = 0.09, 1, 4, 16,$ and 400. An obvious difference is seen for both the upper and lower DCAs between those at high and low Reynolds numbers from Fig. 21. At high Re, the DCA shows an overshoot initially before it gradually reaches a (nearly) constant value. As Re decreases, the amplitude of the overshoot decreases, and it even disappears when Re is low enough (e.g., at $Re = 0.09$). This could be attributed to the inertial effects, which become more significant at high Re. Another observation in DCA is that it shows regular periodic oscillations after the initial adjustment stage: the oscillation frequencies at different Reynolds numbers seem to be close; for all the Reynolds numbers considered, the amplitudes of the oscillation are small (less than 1°). Such oscillations are very likely caused by the *grid roughness effect*[37] and will be revisited later in Subsection III C 12. Finally, it is seen that the DCAs at different Re are very close to each other after the initial adjustment stage.

Next, the effects of the viscosity ratio r_ν are studied while the Reynolds number is fixed at $Re = 16$. Several viscosity ratios, including $r_\nu = 0.1, 0.5, 1, 5, 10, 25,$ and 40, were tested. In order to keep both relaxation parameters $\tau_{f,A}$ and $\tau_{f,B}$ in a suitable range, the temporal discretization parameter N_t was varied for different r_ν. Recall that $S = Pe^{-1/2} r_\nu^{-1/4}$ (see Eq. (30)) and the Peclet number is fixed at $Pe = 5 \times 10^3$. In order to satisfy the condition to achieve the SIL ($Cn_\epsilon < 4S$), the Cahn number has to vary with r_ν. For $r_\nu \leq 1$, we used $Cn = 0.125$ ($Cn_\epsilon = 0.04419$); for $r_\nu > 1$ we used $Cn = 0.0625$ ($Cn_\epsilon = 0.0221$). The smallest value of S (for $r_\nu = 40$) is approximately 5.62×10^{-3}. It is worth noting again that the viscosity ratio is defined as $r_\nu = \nu_A/\nu_B$ (i.e., the kinematic viscosity of the drop (fluid A) over that of the ambient fluid (fluid B)). With a fixed Reynolds number Re, a larger r_ν means a less viscous ambient fluid B. Figure 22 shows the evolutions of the drop velocity v_{drop} at five different viscosity ratios: $r_\nu = 0.1, 0.5, 1, 5,$ and 10. It is obvious that the viscosity of the ambient fluid has a significant effect on the drop motion: increase in r_ν (decrease in ν_B) results in faster motion. Figure 23 shows the variation of the steady capillary number of the drop Ca_{drop} with the viscosity ratio r_ν based on the results obtained at the seven viscosity ratios tested, $r_\nu = 0.1, 0.5, 1, 5, 10, 25,$ and 40. From Fig. 23 we have the following observations: when $r_\nu \leq 1$ the capillary number of the drop Ca_{drop} increases very fast as r_ν becomes larger; in contrast, when r_ν is much larger than unity (e.g., $r_\nu \geq 25$), the rate of increase $\Delta Ca_{\text{drop}}/\Delta r_\nu$ decreases fast as r_ν increases, which seems to indicate an upper limit for Ca_{drop} (found to be approximately 0.03838 based on the exponential fit of the data at $r_\nu = 25$ and 40; see the dashed line in Fig. 23); r_ν between 1 and 25 is a transition region.
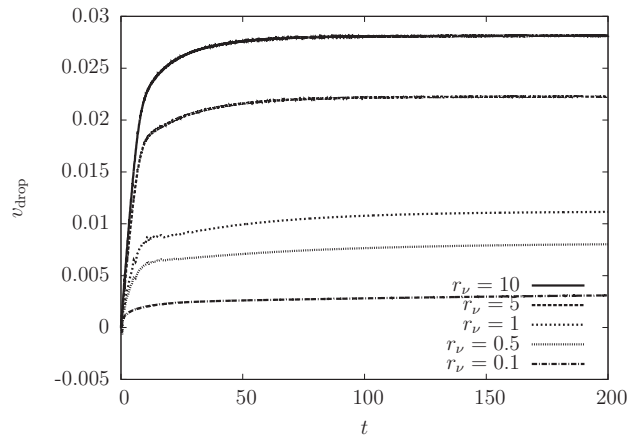
FIG. 22. Evolutions of the centroid velocity of the drop v_{drop} subject to a stepwise WG on a wall at different viscosity ratios $r_\nu = 0.1, 0.5, 1, 5,$ and 10. The common parameters are $Re = 16, \theta^{\text{upp}} = 75°, \theta^{\text{low}} = 105°, \theta_H^{\text{upp}} = \theta_H^{\text{low}} = 0, L_x = 4, L_y = 16, Pe = 5 \times 10^3$.

As before, the DCAs are also examined. Figure 24 compares the evolutions of the DCAs near the upper and lower (Figs. 24(a) and 24(b)) TPPs at the five viscosity ratios as in Fig. 22 ($r_\nu = 0.1, 0.5, 1, 5,$ and 10). A difference is observed for both the upper and lower DCAs between those at high and low viscosity ratios from Fig. 24. At high r_ν (i.e., with less viscous ambient fluid), the DCA shows an overshoot initially before it gradually becomes (almost) constant. As r_ν decreases (i.e., the ambient fluid becomes more viscous), the amplitude of the overshoot decreases, and the overshoot disappears when the ambient fluid is sufficiently viscous (e.g., at $r_\nu = 0.1$). This is likely due to the high viscous damping at small r_ν. As above, the DCAs show regular oscillations after the initial stage, and a less viscous ambient fluid (corresponding to a larger r_ν) makes the oscillation frequency higher. Besides, in the simulations conducted at a smaller Cahn number ($Cn = 0.0625$ for $r_\nu = 5,$ and 10) the oscillation frequencies increase significantly. For all cases, the oscillation amplitudes remain small. As mentioned before, such oscillations are related to the *grid roughness effect*, which can explain the change of the frequency with various factors. More details are given below in Subsection III C 12.

Further investigations on the effects of the Reynolds number at other viscosity ratios led to the same finding that the steady capillary number of the drop Ca_{drop} is (almost) independent of the Reynolds number (for brevity, the details are not shown here). This suggests that Eq. (42) may be
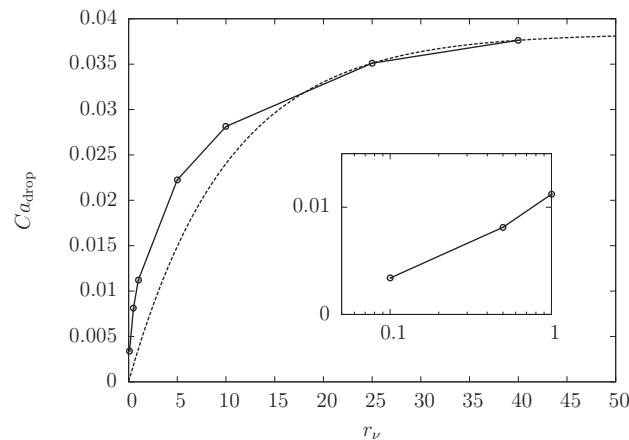
FIG. 23. Variation of the steady capillary number of the drop Ca_{drop} subject to a stepwise WG with the viscosity ratio r_ν. The common parameters are $Re = 16, \theta^{\text{upp}} = 75°, \theta^{\text{low}} = 105°, \theta_H^{\text{upp}} = \theta_H^{\text{low}} = 0, L_x = 4, L_y = 16, Pe = 5 \times 10^3$.
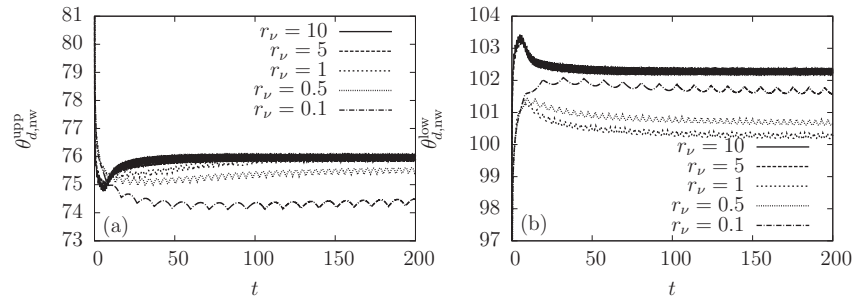
FIG. 24. (a, b) Evolutions of the dynamic contact angles near the upper (a) and lower (b) TPPs (measured at the next-to-outermost layer), $\theta_{d,\text{nw}}^{\text{upp}}$ and $\theta_{d,\text{nw}}^{\text{low}}$, of the drop subject to a stepwise WG at different viscosity ratios $r_v = 0.1, 0.5, 1, 5$, and 10. The common parameters are $Re = 16$, $\theta^{\text{upp}} = 75°$, $\theta^{\text{low}} = 105°$, $\theta_H^{\text{upp}} = \theta_H^{\text{low}} = 0$, $L_x = 4$, $L_y = 16$, $Pe = 5 \times 10^3$.

reduced to

$$Ca_{\text{drop}} = f(r_v, \theta^{\text{upp}}, \theta_H^{\text{upp}}, \theta^{\text{low}}, \theta_H^{\text{low}}). \tag{49}$$

With this equation and the previous relation, $Re_{\text{drop}} = ReCa_{\text{drop}}$, the steady Reynolds number Re_{drop} can be easily obtained once Ca_{drop} is known. For most cases in the present work, Re_{drop} is less than 1 and the inertial effects are not quite significant.

8. Effects of the magnitude of WG

In Eq. (49), in addition to the viscosity ratio r_v there are still four parameters that may affect the capillary number Ca_{drop}, namely, the contact angles of the upper and lower parts, θ^{upp} and θ^{low}, and the magnitudes of the CAH of the two parts, θ_H^{upp} and θ_H^{low}. If there is no CAH (i.e., $\theta_H^{\text{upp}} = \theta_H^{\text{low}} = 0$), two remaining parameters, θ^{upp} and θ^{low}, still play some role. Their effects are studied in this section. As mentioned above, the parameter $\Delta\cos\theta = \cos\theta^{\text{upp}} - \cos\theta^{\text{low}}$ is an important factor to determine the drop motion. Thus, we will not only focus on the individual contact angle, but also on this special parameter $\Delta\cos\theta$. Two groups of the contact angle pair $(\theta^{\text{upp}}, \theta^{\text{low}})$, each containing five pairs, were investigated. In both groups, the parameter $\Delta\cos\theta$ takes one of the following five values: 0.087, 0.259, 0.5, 0.707, and 0.866. In one group, the lower contact angle θ^{low} was fixed to be $\theta^{\text{low}} = 90°$ and the upper one θ^{upp} was varied: $\theta^{\text{upp}} = 85°$, 75°, 60°, 45°, and 30°. In this group, the averages of the two contact angles, $(\theta^{\text{upp}} + \theta^{\text{low}})/2$, are less than 90°, and it is called the hydrophilic group (GL). In the other group, the upper contact angle θ^{upp} was fixed to be $\theta^{\text{upp}} = 90°$, and that on the lower part was varied: $\theta^{\text{low}} = 95°$, 105°, 120°, 135°, and 150°. In this group, the averages of θ^{upp} and θ^{low} are greater than 90°, and it is called the hydrophobic group (GB). The common parameters for all the cases in this part are $Re = 16$, $r_v = 1$, $\theta_H^{\text{upp}} = \theta_H^{\text{low}} = 0$, $L_x = 4$, $L_y = 16$, $Cn = 0.125$, $Pe = 5 \times 10^3$ ($S = 1.414 \times 10^{-2}$), $N_L = 32$, $N_t = 320$.

Figure 25 shows the evolutions of the drop velocity under the above two groups of different combinations of θ^{upp} and θ^{low} on the left wall. Note that the results for $\Delta\cos\theta = 0.087$ are not shown in order to make the legends easy to recognize. It is found from Fig. 25 that, as expected, the velocity in steady state increases as $\Delta\cos\theta$ increases. When $\Delta\cos\theta$ was small (e.g., $\Delta\cos\theta = 0.259$), the velocity seems to be less dependent on the specific values of the upper and lower contact angles (this also holds for another two cases with $\Delta\cos\theta = 0.087$ not shown here). By contrast, at larger $\Delta\cos\theta$ (e.g., $\Delta\cos\theta = 0.5, 0.707, 0.866$), the drop velocity also depends on the specific values of θ^{low} and θ^{upp}. As seen from Fig. 25, after the initial acceleration stage the drop moves faster in the case with $(\theta^{\text{upp}}, \theta^{\text{low}}) = (90°, 150°)$ than in the case with $(\theta^{\text{upp}}, \theta^{\text{low}}) = (30°, 90°)$ though the value of $\Delta\cos\theta$ is the same ($\Delta\cos\theta = 0.866$) for the two cases. This is likely due to that in the case of GB the drop has less contact area with the wall, thus having smaller viscous resistance. Figure 26 shows the shapes of the drop in steady motion for two cases with the same WG ($\Delta\cos\theta = 0.866$) but with different upper and lower contact angles. It is obvious that in the case of GL the drop spreads more on the wall. Another observation from Fig. 25 is that the initial acceleration stage seems to
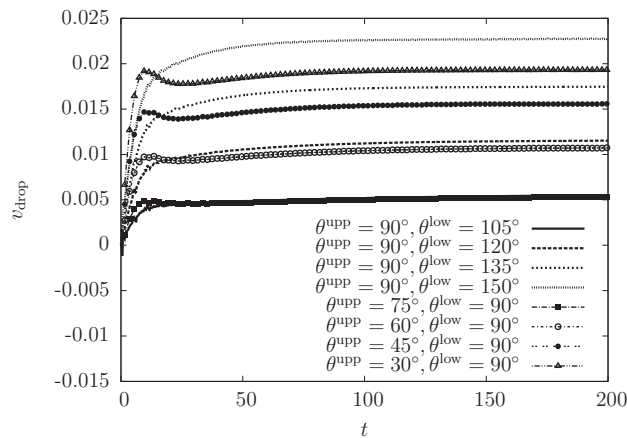
FIG. 25. Evolutions of the centroid velocity of the drop v_{drop} subject to different (stepwise) WGs on a wall. The common parameters are $Re = 16$, $r_v = 1$, $\theta_H^{\text{upp}} = \theta_H^{\text{low}} = 0$, $L_x = 4$, $L_y = 16$, $Cn = 0.125$, $Pe = 5 \times 10^3$ ($S = 1.414 \times 10^{-2}$), $N_L = 32$, $N_t = 320$.

depend on the group (GL or GB), especially at larger $\Delta \cos \theta$: for the hydrophilic group, the drop experienced greater accelerations initially and the drop velocity showed a *bump* before it gradually approached the steady value; by contrast, for the hydrophobic group, the drop was driven towards the steady state smoothly. This could be attributed to the fact that the difference between the initial configuration and the final steady shape of the drop is larger in the cases of GL (see Figs. 11 and 26), thus the drop was accelerated more during the initial adjustment of configuration.

Figure 27 shows the variations the capillary number Ca_{drop} (when the drop is in steady state) with the parameter $\Delta \cos \theta$ for the two groups of simulations. Note that the steady velocity V_{drop} used to calculate Ca_{drop} was taken at different times for different cases to make sure that the criterion in Subsection III C 2 is satisfied. In Fig. 27 we also show the linear fit for the hydrophilic group (GL with $\theta^{\text{low}} = 90°$). From this figure, it is seen that the capillary number Ca_{drop} in steady state almost increases linearly with the magnitude of the WG ($\Delta \cos \theta$) for the hydrophilic group. For the hydrophobic group, the linear relation still roughly holds when $\Delta \cos \theta$ is small; but when the WG magnitude is large, a trend of nonlinear variation is observed and the capillary number becomes slightly larger than that described by the linear variation. The possible reason is already given above: the contact area between the drop and the wall becomes smaller and the viscous resistance is reduced in the hydrophobic group at large $\Delta \cos \theta$.

The present findings agree with that reported by Li *et al.*[62] but seem to contradict those reported by Xu and Qian.[13] In Ref. 13 it was reported that the drop moved faster on the hydrophilic substrate than on the hydrophobic one under "*the same other conditions.*" This contradiction can be most likely attributed to the different definitions of *the same other conditions*. Xu and Qian[13] also considered a 2D drop, but it was driven by a continuous WG with the contact angle θ having a distribution that satisfies $\frac{d(\cos \theta)}{dx} = const$ and $\frac{d(\cos \theta)}{dx} \ll 1$. They mainly looked into the variation of the steady drop
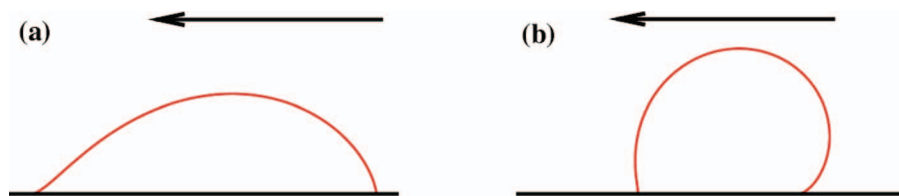
FIG. 26. Drop shapes in steady state for two cases with the same WG ($\Delta \cos \theta = 0.866$): (a) $(\theta^{\text{upp}}, \theta^{\text{low}}) = (30°, 90°)$; (b) $(\theta^{\text{upp}}, \theta^{\text{low}}) = (90°, 150°)$. The common parameters are $Re = 16$, $r_v = 1$, $\theta_H^{\text{upp}} = \theta_H^{\text{low}} = 0$, $L_x = 4$, $L_y = 16$, $Cn = 0.125$, $Pe = 5 \times 10^3$ ($S = 1.414 \times 10^{-2}$), $N_L = 32$, $N_t = 320$. The arrows denote the direction of motion. The figures are rotated by 90° in the anti-clockwise direction.
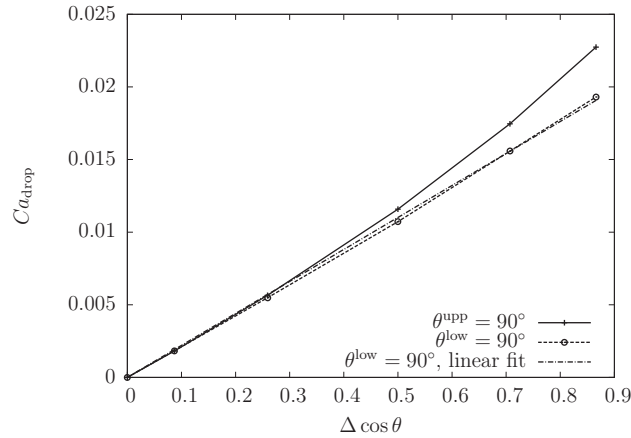
FIG. 27. Variations of the capillary number Ca_{drop} for a drop in steady state subject to different (stepwise) WGs with the magnitude of the WG ($\Delta\cos\theta$). The common parameters are $Re = 16$, $r_v = 1$, $\theta_H^{\mathrm{upp}} = \theta_H^{\mathrm{low}} = 0$, $L_x = 4$, $L_y = 16$, $Cn = 0.125$, $Pe = 5 \times 10^3$ ($S = 1.414 \times 10^{-2}$), $N_L = 32$, $N_t = 320$.

velocity with the parameter $h_0 \frac{\sigma}{\eta} \frac{d\cos\theta}{dx}$ where h_0 is the height of the drop. Consider two drops, one on a hydrophilic surface with the average contact angle being $\theta_1 < 90°$ and the WG being $\frac{d(\cos\theta)}{dx}$ and the other on a hydrophobic surface with the average contact angle being $\theta_2 > 90°$ and the same WG. When they have the same height h_0, they are regarded as under *the same other conditions* according to Xu and Qian.[13] However, the actual driving forces caused by the WG differ because the distances between the two TPPs (about twice of the contact radius R_c in Ref. 13) differ in these two cases. Under a weak WG ($\frac{d(\cos\theta)}{dx} \ll 1$), the drop does not have significant deformations. A straightforward calculation relates the average contact angle θ, the drop height h_0, and the contact radius R_c as follows:

$$R_c = h_0 \frac{\sin\theta}{1 - \cos\theta}. \tag{50}$$

Since the WG satisfies $\frac{d(\cos\theta)}{dx} = const$, the driving force (per unit length, as we are considering 2D problems) $|\boldsymbol{F}_d|$ is found to be

$$|\boldsymbol{F}_d| = \sigma\left[(2R_c)\frac{d(\cos\theta)}{dx}\right] = \sigma\left[\left(2h_0\frac{\sin\theta}{1 - \cos\theta}\right)\frac{d(\cos\theta)}{dx}\right], \tag{51}$$

where the quantity in the square brackets is equivalent to $\Delta\cos\theta$ in the present work. Then, it is easy to find that the ratio of the driving forces in the hydrophilic and hydrophobic cases is

$$\frac{|\boldsymbol{F}_d|_1}{|\boldsymbol{F}_d|_2} = \frac{\sin\theta_1(1 - \cos\theta_2)}{(1 - \cos\theta_1)\sin\theta_2}. \tag{52}$$

Based on the lengths in Fig. 4 of Ref. 13, the two cases they compared were estimated to have $\theta_1 \approx 62.4°$ and $\theta_2 \approx 125.3°$, which gives $\frac{|\boldsymbol{F}_d|_1}{|\boldsymbol{F}_d|_2} \approx 2$. In steady state, with any resistance due to pressure difference or shearing by the ambient fluid being neglected (roughly valid at a large viscosity ratio), the driving force $\boldsymbol{F}_d$ is balanced by (thus equals in magnitude) the viscous resistance force due to the wall (here denoted as $\boldsymbol{F}_{\mathrm{vis,\,w}}$), and with a parabolic velocity profile along each cross section (vertical to the wall) inside the drop being assumed, $|\boldsymbol{F}_{\mathrm{vis,\,w}}|$ is found to be proportional to the steady drop velocity V_{drop} (i.e., $|\boldsymbol{F}_{\mathrm{vis,\,w}}| \propto V_{\mathrm{drop}}$) (for more details, see Ref. 5). Therefore, one has $|\boldsymbol{F}_d| \propto V_{\mathrm{drop}}$. Then, it is not difficult to understand that this factor of 2 found here is quite close to the ratio of the coefficient α_V defined by Xu and Qian[13] (as a measure to reflect how fast the drop moves under certain conditions) for the hydrophilic case over that for the hydrophobic case, which is about 2.06 ($\alpha_V \approx 0.33$, and 0.16 for the hydrophilic and hydrophobic cases respectively[13]). In the present work, one of the requirements for two cases to be under *the same other conditions* is that the driving forces

(or equivalently, the magnitudes of the stepwise WG) are equal (rather than any others based on the height of the drop).

9. Effects of the CAH

In the above, all the factors in Eq. (49) have been studied except the magnitude of the CAH, $\theta_H^{\text{upp}} = \theta_A^{\text{upp}} - \theta_R^{\text{upp}}$, and $\theta_H^{\text{low}} = \theta_A^{\text{low}} - \theta_R^{\text{low}}$. In this part, we consider the effects of the CAH. By exploring different parameter regimes, we find (at least) three different situations. In the first, there is *no notable contact line pinning*; in the second, contact line pinning is observed on both the upper and lower parts and the drop almost remains stationary completely; in the third, contact line pinning occurs only on one of the two parts (either lower or upper).

The first two situations are presented first. For simplicity, we only study the cases with $\theta_H^{\text{upp}} = \theta_H^{\text{low}} = \theta_H$. Two sets of upper and lower contact angles are considered: (S1) $\theta^{\text{upp}} = 75°, \theta^{\text{low}} = 105°$; (S2) $\theta^{\text{upp}} = 60°, \theta^{\text{low}} = 120°$. The Reynolds number and the viscosity ratio are fixed at $Re = 16$ and $r_v = 1$. The remaining parameters are $L_x = 4, L_y = 16, Cn = 0.125, Pe = 5 \times 10^3$ ($S = 1.414 \times 10^{-2}$), $N_L = 32, N_t = 320$. In each of the two sets, S1 and S2, three magnitudes of CAH were tried in addition to the cases with no CAH (i.e., $\theta_H = 0$). In S1, $\theta_H = 4°, 10°$, and $30°$, and in S2, $\theta_H = 20°, 40°$, and $60°$. Thus, we have the following pairs of advancing and receding contact angles for the upper and lower parts in S1,

- (S1a) $\theta_{A,R}^{\text{upp}} = 77°, 73°, \theta_{A,R}^{\text{low}} = 107°, 103°$,
- (S1b) $\theta_{A,R}^{\text{upp}} = 80°, 70°, \theta_{A,R}^{\text{low}} = 110°, 100°$,
- (S1c) $\theta_{A,R}^{\text{upp}} = 90°, 60°, \theta_{A,R}^{\text{low}} = 120°, 90°$,

and in S2 we have

- (S2a) $\theta_{A,R}^{\text{upp}} = 70°, 50°, \theta_{A,R}^{\text{low}} = 130°, 110°$,
- (S2b) $\theta_{A,R}^{\text{upp}} = 80°, 40°, \theta_{A,R}^{\text{low}} = 140°, 100°$,
- (S2c) $\theta_{A,R}^{\text{upp}} = 90°, 30°, \theta_{A,R}^{\text{low}} = 150°, 90°$.

Figure 28 shows the evolutions of the drop velocity v_{drop} in the four cases with different θ_H in S1. It is found from Fig. 28 that when the CAH was not too large ($\theta_H = 4°$ for Case (S1a)), and $\theta_H = 10°$ for Case (S1b)) the drop accelerated initially and then gradually showed a trend to become steady. This behavior is just like the reference case with no CAH and the difference is that the velocity is reduced when CAH is present, as expected. When the CAH was large enough ($\theta_H = 30°$ for Case (S1c)), the drop almost remained static. This is because in Case (S1c) the initial drop shape
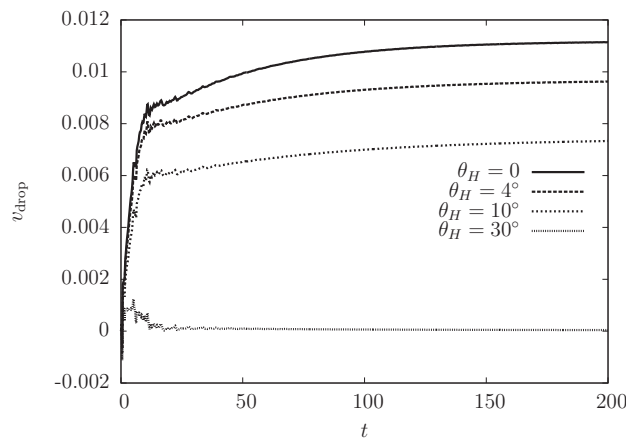
FIG. 28. Evolutions of the centroid velocity of the drop v_{drop} subject to a stepwise WG on a wall with CAH of (S1a) $\theta_H = 4°$ ($\theta_{A,R}^{\text{upp}} = 77°, 73°, \theta_{A,R}^{\text{low}} = 107°, 103°$); (S1b) $\theta_H = 10°$ ($\theta_{A,R}^{\text{upp}} = 80°, 70°, \theta_{A,R}^{\text{low}} = 110°, 100°$); (S1c) $\theta_H = 30°$ ($\theta_{A,R}^{\text{upp}} = 90°, 60°, \theta_{A,R}^{\text{low}} = 120°, 90°$). Also shown is the case with no CAH ($\theta_H = 0°$). The common parameters are $Re = 16, r_v = 1, L_x = 4, L_y = 16, Cn = 0.125, Pe = 5 \times 10^3$ ($S = 1.414 \times 10^{-2}$), $\theta^{\text{upp}} = 75°, \theta^{\text{low}} = 105°, N_L = 32, N_t = 320$.
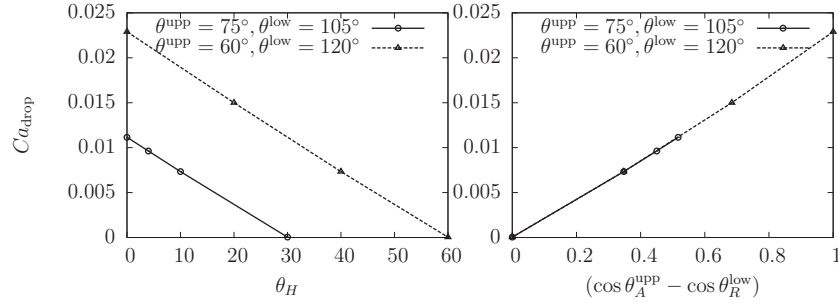
FIG. 29. Variation of the steady capillary number Ca_{drop} of a drop subject to a stepwise WG on a wall with CAH with the magnitude of the CAH (θ_H) (left) and the parameter $(\Delta\cos\theta)_H = \cos\theta_A^{\mathrm{upp}} - \cos\theta_R^{\mathrm{low}}$ (right) for two sets with (S1) $\theta^{\mathrm{upp}} = 75°, \theta^{\mathrm{low}} = 105°$; (S2) $\theta^{\mathrm{upp}} = 60°, \theta^{\mathrm{low}} = 120°$. The common parameters are $Re = 16, r_v = 1, L_x = 4, L_y = 16, Cn = 0.125, Pe = 5 \times 10^3$ ($S = 1.414 \times 10^{-2}$), $N_L = 32, N_t = 320$.

is within the range of the equilibrium states allowed by the given advancing and receding contact angles ($\theta^{\mathrm{i}} = \theta_A^{\mathrm{upp}} = \theta_R^{\mathrm{low}} = 90°$). In the other set of simulations (S2) we have similar observations.

Figure 29 plots the variations of the steady capillary number Ca_{drop} with the magnitude of the CAH (θ_H) (left panel) and also with another quantity $(\Delta\cos\theta)_H = \cos\theta_A^{\mathrm{upp}} - \cos\theta_R^{\mathrm{low}}$ (right panel) for the two sets (S1 and S2). It is found from the left panel of Fig. 29 that the steady capillary number Ca_{drop} decreases as the magnitude of the hysteresis (θ_H) increases, and the data points of the pair ($Ca_{\mathrm{drop}}, \theta_H$) almost fall on a straight line for each set. Besides, the two lines for S1 and S2 appear to be parallel. From the right panel of Fig. 29 it is seen that Ca_{drop} increases roughly linearly with the quantity $(\Delta\cos\theta)_H$ and the data points for both sets are almost on the same straight line. These results suggest that for a (2D) drop on a substrate with a stepwise WG and CAH, the most important factors are the advancing contact angle of the more hydrophilic region and the receding contact angle of the more hydrophobic region, which somehow defines the equivalent magnitude of the WG in the presence of CAH.

Next, we present the third situation with contact line pinning on one part only. The above results indicate that θ_A^{upp} and θ_R^{low} are two determinant factors. As one can see, in the above two situations the initial contact angle θ^{i} satisfies $\theta_R^{\mathrm{low}} \geq \theta^{\mathrm{i}} \geq \theta_A^{\mathrm{upp}}$. Unlike these two situations, in the third we have $\theta^{\mathrm{i}} > \theta_R^{\mathrm{low}} > \theta_A^{\mathrm{upp}}$ (R1) or $\theta_R^{\mathrm{low}} > \theta_A^{\mathrm{upp}} > \theta^{\mathrm{i}}$ (R2). The common parameters for the new cases are $Re = 16, r_v = 1, L_x = 4, L_y = 16, Cn = 0.125, Pe = 5 \times 10^3$ ($S = 1.414 \times 10^{-2}$), $N_L = 32, N_t = 320$. For R1, we did more thorough studies whereas only one case was considered for R2 (because R2 is quite similar to R1 in many aspects except the pinning occurs at a different place). For R1 the lower contact angle and the parameter that characterizes the CAH on the upper part are $\theta^{\mathrm{low}} = 90°, \theta_H^{\mathrm{upp}} = 10°$, whereas for R2 the lower contact angle and the parameter for CAH on the lower part are $\theta^{\mathrm{upp}} = 90°, \theta_H^{\mathrm{low}} = 10°$. Other parameters for the case in R2 are $\theta^{\mathrm{low}} = 140°, \theta_H^{\mathrm{upp}} = 40°$, which give the following pairs of advancing and receding angles for the upper and lower parts: $(\theta_A^{\mathrm{upp}}, \theta_R^{\mathrm{upp}}) = (110°, 70°), (\theta_A^{\mathrm{low}}, \theta_R^{\mathrm{low}}) = (145°, 135°)$. In R1, two sets are studied in order to examine the effects of θ_R^{low} and θ_A^{upp}, respectively. In one set, the upper contact angle is fixed at $\theta^{\mathrm{upp}} = 40°$ ($(\theta_A^{\mathrm{upp}}, \theta_R^{\mathrm{upp}}) = (45°, 35°)$) whereas θ_H^{low} takes the following values: $\theta_H^{\mathrm{low}} = 20°, 30°, 40°, 50°$, and $70°$, which correspond to the following pairs of advancing and receding angles on the lower part: $(\theta_A^{\mathrm{low}}, \theta_R^{\mathrm{low}}) = (100°, 80°), (105°, 75°), (110°, 70°), (115°, 65°)$, and $(125°, 55°)$. In the other set, θ_H^{low} is fixed at $40°$ ($(\theta_A^{\mathrm{low}}, \theta_R^{\mathrm{low}}) = (110°, 70°)$) whereas the upper contact angle θ^{upp} takes these values: $\theta^{\mathrm{upp}} = 35°, 40°, 45°, 50°$, and $55°$, which correspond to the following pairs of advancing and receding angles on the upper part: $(\theta_A^{\mathrm{upp}}, \theta_R^{\mathrm{upp}}) = (40°, 30°), (45°, 35°), (50°, 40°), (55°, 45°)$, and $(60°, 50°)$. First, the common case shared by the two sets in R1 with $(\theta_A^{\mathrm{upp}}, \theta_R^{\mathrm{upp}}) = (45°, 35°)$ and $(\theta_A^{\mathrm{low}}, \theta_R^{\mathrm{low}}) = (110°, 70°)$ and the (single) case in R2 with $(\theta_A^{\mathrm{upp}}, \theta_R^{\mathrm{upp}}) = (110°, 70°)$ and $(\theta_A^{\mathrm{low}}, \theta_R^{\mathrm{low}}) = (145°, 135°)$ are examined in detail. Figure 30 shows the temporal evolutions of the positions and velocities of the advancing and receding CLs (ACL and RCL) as well as the local contact angle at the RCL (for the case in R1) or at the ACL (for the case in R2) *on the wall* for the two selected cases. From the left column (for the case in R1)
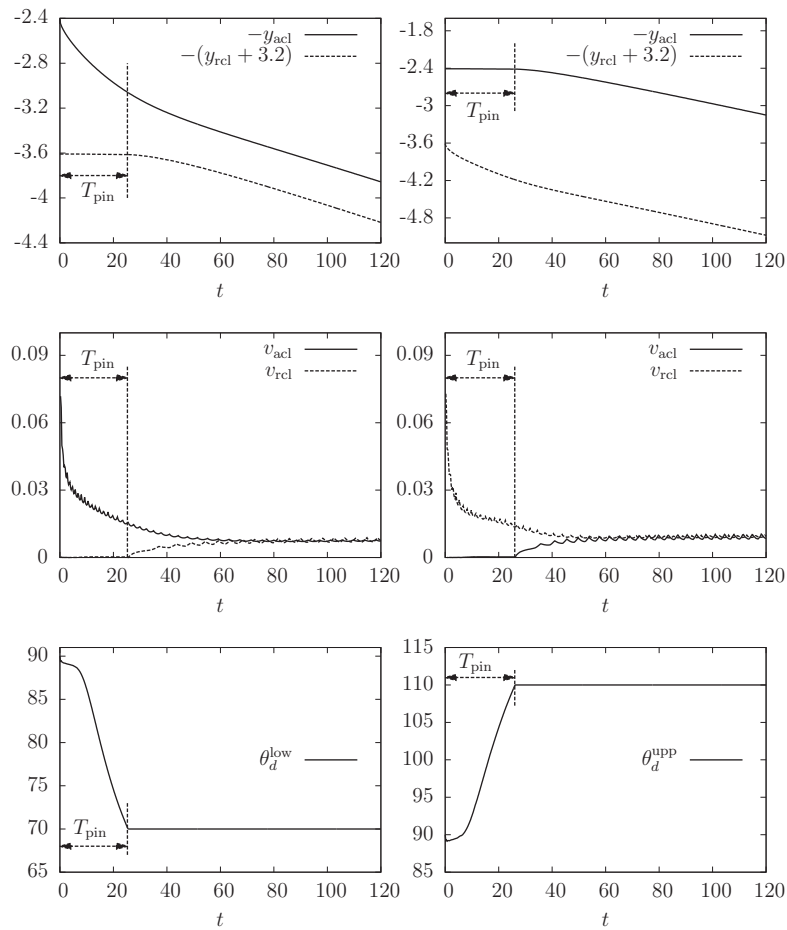
FIG. 30. Evolutions of the positions (upper row) and velocities (middle row) of the advancing and receding CLs (ACL and RCL) and the local contact angle at the RCL or ACL *on* the wall (lower row) for two cases with $(\theta_A^{\mathrm{upp}}, \theta_R^{\mathrm{upp}}) = (45^\circ, 35^\circ)$, $(\theta_A^{\mathrm{low}}, \theta_R^{\mathrm{low}}) = (110^\circ, 70^\circ)$ (left column) and with $(\theta_A^{\mathrm{upp}}, \theta_R^{\mathrm{upp}}) = (110^\circ, 70^\circ)$, $(\theta_A^{\mathrm{low}}, \theta_R^{\mathrm{low}}) = (145^\circ, 135^\circ)$ (right column). The common parameters are $Re = 16$, $r_\nu = 1$, $L_x = 4$, $L_y = 16$, $Cn = 0.125$, $Pe = 5 \times 10^3$ ($S = 1.414 \times 10^{-2}$), $N_L = 32$, $N_t = 320$.

of Fig. 30 it is seen that while the ACL moves as in other cases that have been studied before, the RCL almost remains stationary (i.e., pinned) during the period $t < T_{\mathrm{pin}}$ ($T_{\mathrm{pin}} = 25.25$ for this case); it starts to move only after $t = T_{\mathrm{pin}}$ when the local contact angle near the RCL has adjusted from the initial value of 90°–70° (the receding angle θ_R^{low} on the lower part). Note that in Fig. 30 the positions of the ACL and RCL are brought closer artificially: we plotted $-y_{\mathrm{acl}}$ and $-(y_{\mathrm{rcl}} + 3.2)$, instead of y_{acl} and y_{rcl}, in Fig. 30. Through this transformation, the upper-left panel of Fig. 30 appears similar to some portion of Fig. 4 in Ref. 15, which showed the evolutions of the positions of two contact lines of a ridge driven by a stepwise WG on a surface with CAH as recorded in their experiments. Here we do not intend to make quantitative comparisons with their experimental data because the current problem setting differs in many aspects and it is difficult to perform simulations under exactly the same condition (e.g., the slip length in reality is too small to be resolved); we mainly want to highlight that the different stages of drop motion caused by the contact line pinning are captured in the present simulation. In the right column (for the case in R2) of Fig. 30 one has similar observations except that the ACL (instead of the RCL) is pinned for $t < T_{\mathrm{pin}}$ ($T_{\mathrm{pin}} = 26$ for this case), and it starts to move from $t = T_{\mathrm{pin}}$ when the local contact angle near the ACL increases from the initial value of 90° to 110° (the advancing angle θ_A^{upp} on the upper part). Figure 31 shows the interfaces at selected times for the two cases, including the initial stage when the RCL or ACL is pinned ($t = 0, 10, 20$) and the subsequent stage when it is in motion ($t = 30, 50$). From Fig. 31
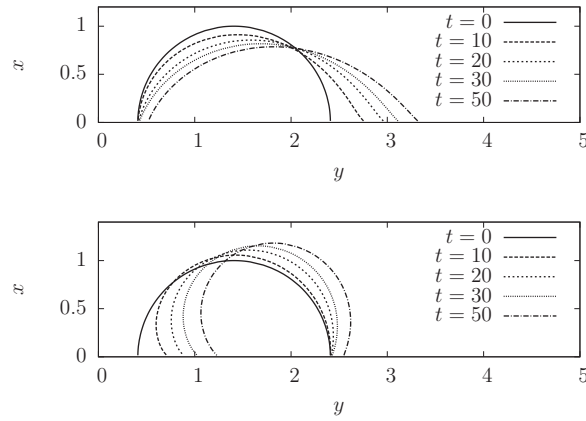
FIG. 31. Snapshots of the interfaces at selected times for a drop driven by a stepwise WG for two cases with $(\theta_A^{\mathrm{upp}}, \theta_R^{\mathrm{upp}}) = (45°, 35°)$, $(\theta_A^{\mathrm{low}}, \theta_R^{\mathrm{low}}) = (110°, 70°)$ (upper panel) and with $(\theta_A^{\mathrm{upp}}, \theta_R^{\mathrm{upp}}) = (110°, 70°)$, $(\theta_A^{\mathrm{low}}, \theta_R^{\mathrm{low}}) = (145°, 135°)$ (lower panel). Note that the figures have been transformed to make the x-axis point upwards and the y-axis point rightwards. The other parameters are the same as in Fig. 30.

one can directly observe how the drop deforms as the surface tension pulls the ACL (or pushes the RCL) and finally makes the RCL (or ACL) move. In addition to the analyses of this specific case, we have also checked the time for the RCL to remain pinned on the wall (T_{pin}) in R1 at different upper contact angles (θ^{upp}) and different magnitudes of low CAH (θ_H^{low}). Through some physical analyses, one may expect that T_{pin} is affected by the three angles mentioned above: (1) the initial contact angle θ^{i}; (2) the receding angle of the lower part θ_R^{low}; (3) the advancing angle of the upper part θ_A^{upp}. The difference between θ^{i} and θ_R^{low} reflects the gap between the initial condition and the state when the RCL starts to move. The upper advancing angle θ_A^{upp} determines, to some extent, the magnitude of the driving force. Figure 32 gives the variation of T_{pin} with $\theta^{\mathrm{i}} - \theta_R^{\mathrm{low}}$ and $\theta_R^{\mathrm{low}} - \theta_A^{\mathrm{upp}}$ as obtained from the cases in the above two sets in R1, with θ^{i} fixed and θ_R^{low} varying and with θ_R^{low} fixed and θ_A^{upp} varying, respectively. As found in Fig. 32, T_{pin} increases as $\theta^{\mathrm{i}} - \theta_R^{\mathrm{low}}$ becomes larger (the larger the gap is, the more time is required for the RCL to move) whereas it decreases as $\theta_R^{\mathrm{low}} - \theta_A^{\mathrm{upp}}$ increases (the larger the driving force is, the less time is required); besides, T_{pin} seems to show an exponential increase at large $\theta^{\mathrm{i}} - \theta_R^{\mathrm{low}}$.

10. Analyses of the overall flow field and velocity profile

Finally, we examine some details of the flow when the drop reaches steady state. For this purpose, we select a few typical cases with $Re = 16$, $\theta^{\mathrm{upp}} = 75°$, $\theta^{\mathrm{low}} = 105°$, $\theta_H^{\mathrm{upp}} = \theta_H^{\mathrm{low}} = 0$, and
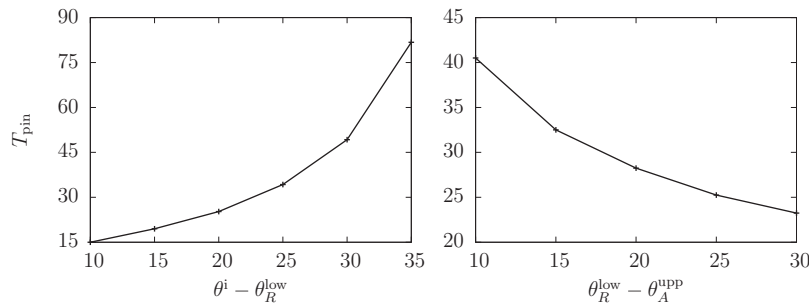
FIG. 32. Variation of the time for the receding contact line to be pinned on the wall T_{pin} with the difference between the initial contact angle θ^{i} and the receding angle of the lower part θ_R^{low}, $\theta^{\mathrm{i}} - \theta_R^{\mathrm{low}}$, and with the difference between θ_R^{low} and the upper advancing contact angle θ_A^{upp}, $\theta_R^{\mathrm{low}} - \theta_A^{\mathrm{upp}}$. The left panel is obtained with θ^{i} fixed and θ_R^{low} varying whereas the right is obtained with θ_R^{low} fixed and θ_A^{upp} varying. The specific parameters are given in the text.
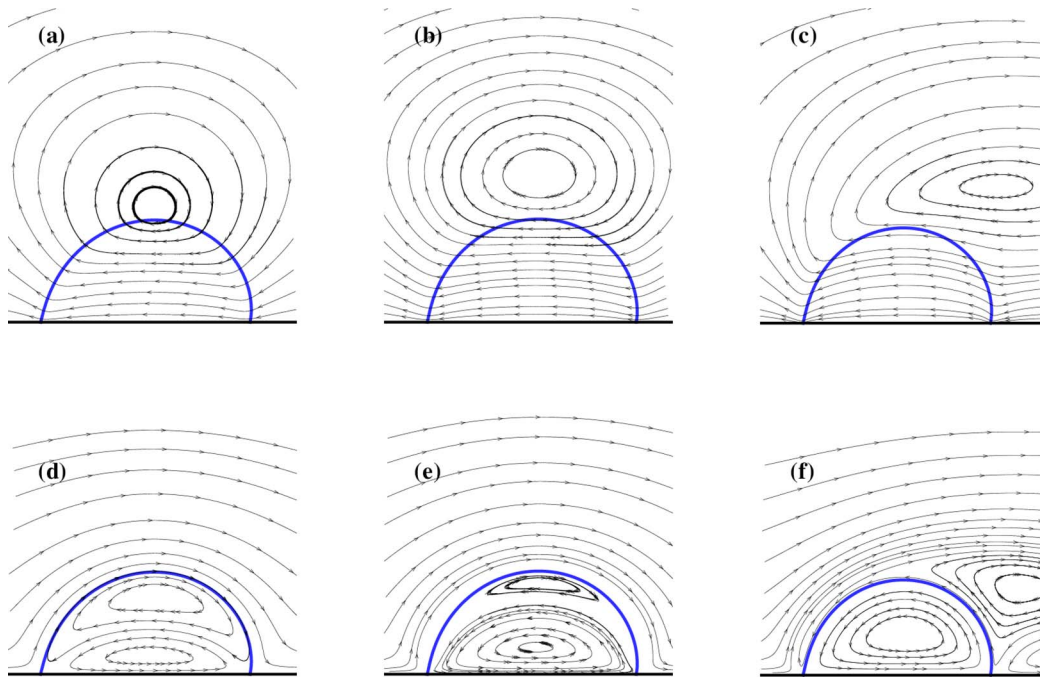
FIG. 33. Drop shapes and streamlines around the drop subject to a stepwise WG at $r_v = 0.1, 1$, and 40 (left, middle, and right columns, respectively). The upper row shows streamlines as observed in the frame fixed on the wall whereas the lower row shows those observed in the frame moving with the drop. The common parameters are $Re = 16$, $\theta^{\text{upp}} = 75°$, $\theta^{\text{low}} = 105°$, $\theta_H^{\text{upp}} = \theta_H^{\text{low}} = 0$, $L_x = 4$, $L_y = 16$, $Pe = 5 \times 10^3$. The figures are rotated by 90° in the anti-clockwise direction.

the following viscosity ratios: $r_v = 0.1, 1, 5$, and 40. Other common parameters are $L_x = 4$, $L_y = 16$, $Pe = 5 \times 10^3$ ($S = 1.414 \times 10^{-2}$).

Figure 33 shows the drop shapes and the streamlines around the drop (from left to right: (a, d) for $r_v = 0.1$ at $t = 600$, (b, e) for $r_v = 1$ at $t = 400$, and (c, f) for $r_v = 40$ at $t = 200$) as observed in two different frames: the frame fixed on the wall denoted as the *absolute frame* shown in the upper row, and the frame moving with the drop denoted as the *relative frame* shown in the lower row. From the upper row in Fig. 33, when the observation is made in the *absolute* frame, a circulation is seen with its center being close to but above the top of drop. As the viscosity ratio r_v increases, the circulation center first moves upwards and then moves downstream. Besides, the streamlines pass through the drop and were slightly bent when crossing the interfaces. If the observation is made in the *relative* frame, the streamlines show distinctive patterns, as found in the lower row of Fig. 33. The most noticeable feature is that two circulation regions form, with one above the other. At low viscosity ratios (i.e., the ambient fluid is more viscous), both circulations are inside the drop, but the upper one covers a larger area than the lower one at $r_v = 0.1$ whereas the opposite is true at $r_v = 1$. At a high viscosity ratio ($r_v = 40$), the upper circulation forms outside the drop and the lower one almost occupies the whole inner area of the drop. It is suspected that the above change of streamline pattern is not only caused by the change of the viscosity ratio, but also (probably more likely) caused by the change of the actual Reynolds number Re_{drop} ($Re_{\text{drop}} = 0.054, 0.18$, and 0.60 for $r_v = 0.1, 1$, and 40, respectively).

In addition, we examine the profile of the (absolute) velocity component v in steady state along the horizontal line passing through the top of the drop. Four cases with different viscosity ratios, $r_v = 0.1, 1, 5$, and 40, are examined with other common parameters already given above. Figure 34 compares the profiles of $v(x)$ for the four cases. Note that the x-axis is put as in its normal position in Fig. 34 without any rotation (unlike in Fig. 33), and the velocity is measured in the characteristic velocity U_c. It is seen that in all cases the profiles $v(x)$ along the selected lines inside the drop (on the left of the short dashed vertical lines) resemble that of a Poiseuille flow, but the points of inflection, where the maximum velocities occur, are below (i.e., on the left of) the top of the drop.
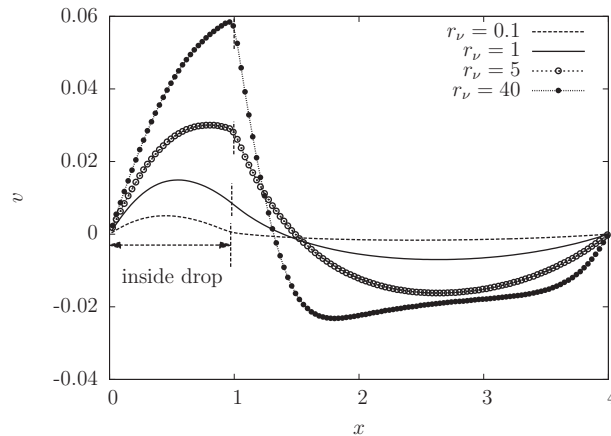
FIG. 34. The profiles of the (absolute) velocity component $v(x)$ along the horizontal line passing through the top of the drop in steady state for four cases with different viscosity ratios, $r_\nu = 0.1, 1, 5$, and 40. The common parameters are $Re = 16$, $\theta^{\rm upp} = 75°$, $\theta^{\rm low} = 105°$, $\theta_H^{\rm upp} = \theta_H^{\rm low} = 0$, $L_x = 4$, $L_y = 16$, $Pe = 5 \times 10^3$. The short dashed vertical lines denote the positions of the top of the drop for the four cases, which differ slightly.

When the viscosity ratio is relatively low ($r_\nu = 0.1, 1$, and 5), the point of inflection is relatively farther away from the top of the drop (the lower r_ν is, the farther). The profile at $r_\nu = 0.1$ (i.e., when the ambient fluid is ten times more viscous than the drop) appears to be the closest to a full Poiseuille profile among all cases. The observation on the inflection point at $r_\nu = 5$ seems to agree with that reported by Xu and Qian,[13] in which the viscosity ratio was about 5. In contrast, the point of inflection becomes very close to the top of the drop at a large viscosity ratio ($r_\nu = 40$), making the profile inside the drop look like half of the full Poiseuille profile. This observation supports the previous assumption about the velocity profile made by Brochard[5] for the derivation of theoretical results.

11. Flow near the contact line and the slip length

In addition to the overall flow, we have also checked the flow near the contact line. Two cases are selected for this purpose. The common parameters are $Re = 16$, $\theta^{\rm upp} = 75°$, $\theta^{\rm low} = 105°$, $\theta_H^{\rm upp} = \theta_H^{\rm low} = 0$, $L_x = 4$, $L_y = 16$, $Cn = 0.0625$, $Pe = 5 \times 10^3$, $N_L = 64$, $N_t = 2560$. In one case, the viscosity ratio is $r_\nu = 1$ and the diffusion length is $l_d = 1.414 \times 10^{-2}$; in the other, $r_\nu = 10$ and $l_d = 7.95 \times 10^{-3}$. Figure 35 shows the streamlines near the ACL for the two cases as observed in the frame moving with the ACL. As seen from this figure, the wedge flow pattern (see Refs. 23, 63) is observed in both cases and look similar to previous findings by Jacqmin[38] and by Yue, Zhou, and Feng[27] although the flow in their work was driven by other means instead of a stepwise WG (e.g., by a moving wall in Ref. 38 or by Poiseuille flow in Ref. 27). The small dot in Fig. 35 denotes the stagnation point with $u \approx 0$ and $v - v_{\rm acl} \approx 0$. Note that in Fig. 35 the wall is located $h/2$ away from the outmost grid line (for clarity, the mesh is not shown). The distance between the stagnation point and the wall, which may be regarded as the slip length l_s,[27] was found to be 0.0346 for $r_\nu = 1$ ($l_d = 1.414 \times 10^{-2}$) and 0.0194 for $r_\nu = 10$ ($l_d = 7.95 \times 10^{-3}$), respectively. Both follow the correlation found by Yue, Zhou, and Feng:[27] $l_s = 2.5l_d$ (for $l_d = 1.414 \times 10^{-2}$, $2.5l_d \approx 0.0354$ and for $l_d = 7.95 \times 10^{-3}$, $2.5l_d \approx 0.0199$). Besides, the stagnation point at the large viscosity ratio, $r_\nu = 10$, moves towards the ambient fluid (which is less viscous) as compared with that at $r_\nu = 1$. Similar observation on this kind of migration was reported by Yue, Zhou, and Feng.[27]

12. On the oscillations during the motion of the contact lines

It has been observed from the above results that not only the dynamic contact angle near the wall $\theta_{d,\rm nw}$ but also the contact line velocity on the wall V_{cl} (when scaled by U_c, it is the capillary number based on V_{cl}, $Ca_{\rm cl}$) oscillated (at a small amplitude) even when the drop velocity reached
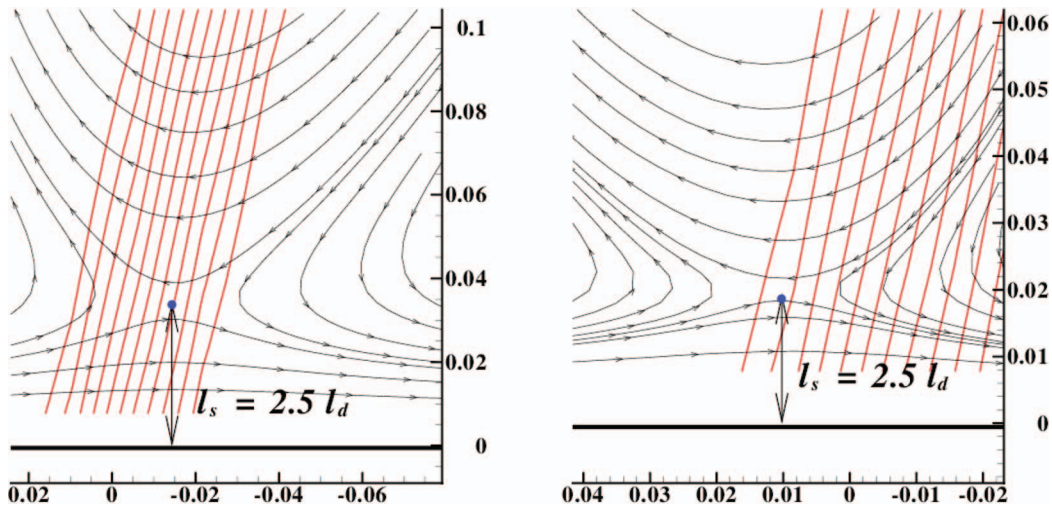
FIG. 35. The streamlines near the advancing contact line (ACL) as observed in the frame moving with the ACL (left panel: $r_v = 1$, $l_d = 1.414 \times 10^{-2}$; right panel: $r_v = 10$, $l_d = 7.95 \times 10^{-3}$). The common parameters are $Re = 16$, $\theta^{\text{upp}} = 75°$, $\theta^{\text{low}} = 105°$, $\theta_H^{\text{upp}} = \theta_H^{\text{low}} = 0$, $L_x = 4$, $L_y = 16$, $Cn = 0.0625$, $Pe = 5 \times 10^3$, $N_L = 64$, $N_t = 2560$, and both plots are taken at $t = 200$. The parallel lines are the contour lines for $-0.6 \leq \phi \leq 0.6$ (with an increment of 0.1). The figures have been rotated by 90° in the anti-clockwise direction. In each plot, the coordinate in the horizontal direction is relative to the respective position of the ACL (i.e., it denotes $y - y_{\text{acl}}$).

the steady stage. Besides, careful examinations of the oscillations of $\theta_{d,\text{nw}}$ and Ca_{cl} reveal that they are well synchronized. Further analyses indicate that such oscillations do not seem to have physical origins (i.e., they are not related to the characteristic frequency of the drop). Instead, they are very probably related to the *grid roughness effect*, which was briefly studied by Jacqmin[37] for phase-field simulation of two-phase flows (perhaps the first study of this kind). As pointed out by Jacqmin,[37] the use of a discrete grid in numerical simulations causes a spatial roughness, and an interface that moves through it shows small oscillations similar to a real interface moving on a surface with certain roughness. The ultimate cause can be traced to the difference in the approximation errors of the spatial gradients (e.g., $\nabla \phi$) when the interface (where $\phi = 0$) is located at different positions in a grid (for instance, at the cell center and at the cell interface if a simple 1D interface is considered). Numerical schemes for the evaluation of spatial gradients always have certain errors embedded. In phase-field simulations, the magnitude of the gradient $|\nabla \phi|$ is usually very large at the interface. Even at a separation distance of half grid size $h/2$, the difference in the numerical errors could be significant, leading to a small artificial oscillation. To confirm that the grid roughness effect causes the oscillations, a straightforward way is to plot the change of the respective variable with the contact line position. We studied the oscillations for three sets of simulations at different viscosity ratios, different pairs of the upper and lower contact angles and different Cahn numbers with these common parameters $Re = 16$, $\theta_H^{\text{upp}} = \theta_H^{\text{low}} = 0$, $L_x = 4$, $L_y = 16$, $Pe = 5 \times 10^3$. Figure 36 shows the variations of the capillary number of the advancing contact line Ca_{acl}, including its temporal evolutions and its spatial variation near the end of the simulation ($t = 200$). In the plots of its spatial variation, the spatial coordinates are in units of the respective grid size h ($h = 1/32$ for $Cn = 0.125$ and $h = 1/64$ for $Cn = 0.0625$). As found from the left column of Fig. 36, the oscillation frequency of Ca_{acl} varies with all the factors (the viscosity ratio r_v, contact angles (θ^{upp}, θ^{low}), and Cahn number Cn). In the present work the grid points are located at $((i - 0.5)h, (j - 0.5)h)$ (i and j are positive integers). From the right column of Fig. 36, one can find that the oscillation has a wavelength h irrespective of any of the factors: r_v, (θ^{upp}, θ^{low}), or Cn.

Based on the above knowledge of the grid roughness effect, one may expect that it would become less significant as the approximation error of the spatial gradient decreases. This was actually demonstrated by Jacqmin[37] for a 1D interface. Here we also verify this for the drop driven by the imposed WG. By increasing the ratio of the interface thickness W over the grid size h, one
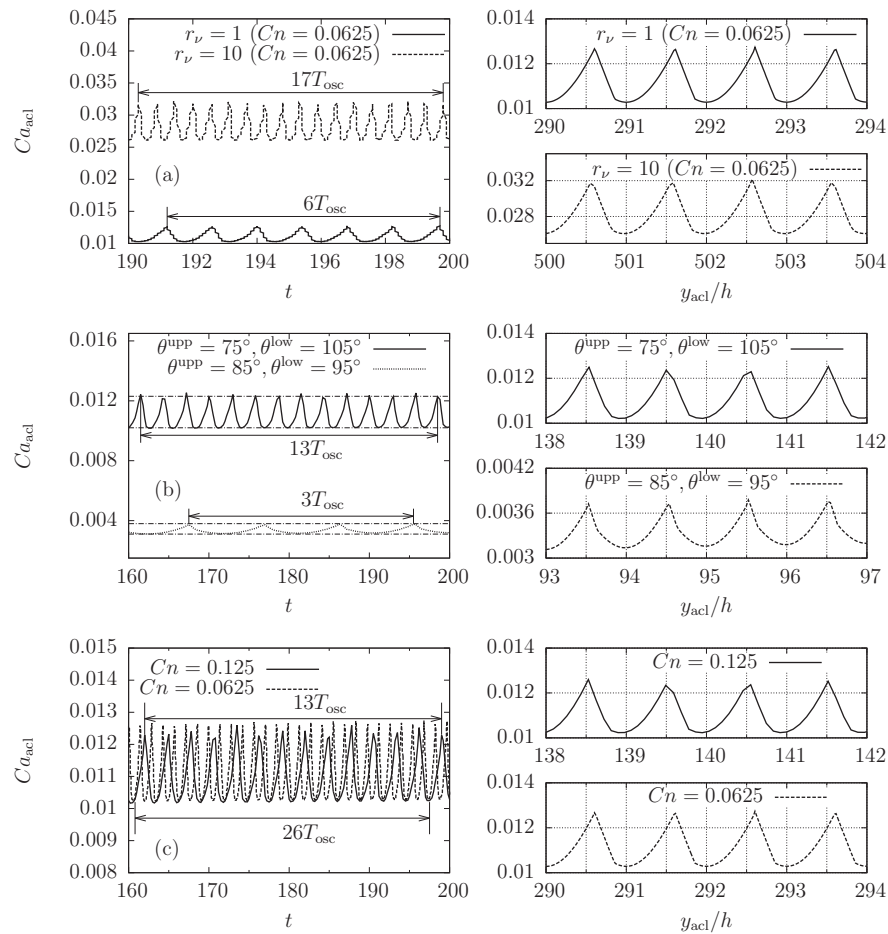
FIG. 36. Variations of the capillary number of the advancing contact line Ca_{acl} near the end of the simulation ($t = 200$) under different parameters (left column: variation of Ca_{acl} with time t; right column: variation of Ca_{acl} with the advancing contact line position y_{acl}/h): (a) at two viscosity ratios $r_\nu = 1$ and 10 (both at $Cn = 0.0625$); (b) at two pairs of upper and lower contact angles $(\theta^{upp}, \theta^{low}) = (75°, 105°)$ and $(85°, 95°)$; (c) at two Cahn numbers $Cn = 0.125$ and 0.0625. The common parameters are $Re = 16$, $\theta_H^{upp} = \theta_H^{low} = 0$, $L_x = 4$, $L_y = 16$, $Pe = 5 \times 10^3$.

allows the interface to span more grid points (i.e., the profile of ϕ across the interface is better resolved), thus reducing the approximation error (and, most likely, also reducing the difference in the error). Figure 37 compares the evolutions of Ca_{acl} for two simulations of the case with $Re = 16$, $r_\nu = 1$, $(\theta^{upp}, \theta^{low}) = (75°, 105°)$, $\theta_H^{upp} = \theta_H^{low} = 0$, $L_x = 4$, $L_y = 16$, $Cn = 0.125$, $Pe = 5 \times 10^3$ at different W/h ($W/h = 4$ and 8). The discretization parameters for $W/h = 4$ are $N_L = 32$, $N_t = 320$, whereas those for $W/h = 8$ are $N_L = 64$, $N_t = 2560$. It is obvious from Fig. 37 that at $W/h = 8$ the oscillation amplitude is much reduced. It is also seen that the oscillation is still present at $W/h = 8$ and the wavelength is still equal to the grid size h (see the right panel of Fig. 37). At the same time, it should be mentioned that the computational cost for $W/h = 8$ increased by more than tenfold. Thus, here one faces again the issue of making a compromise between the computational cost and the accuracy (plus the associated grid roughness effect). When the main focus is on the large scale drop motion, these oscillations may not be so disturbing. If one needs very accurate details of the contact line motion, it is very desirable to reduce as much as possible such artificial oscillations as they may interfere with the physical interface movement. The use of adaptive mesh refinement can help to improve the accuracy without significantly increasing the cost (we would leave the relevant development for future).

   In the literature, the studies of the grid roughness effect on the motion of contact lines seem to be rather rare. Many previous studies on phase-field (diffuse-interface) simulations involving contact
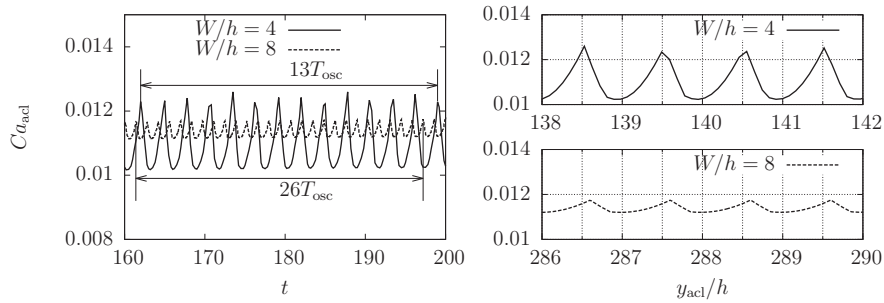
FIG. 37. (a, b) Variations of the capillary number of the advancing contact line Ca_{acl} near the end of the simulation ($t = 200$) under different W/h ($W/h = 4$ and 8) (left: variation of Ca_{acl} with time t; right: variation of Ca_{acl} with the advancing contact line position y_{acl}/h). The common parameters are $Re = 16$, $r_v = 1$, $(\theta^{upp}, \theta^{low}) = (75°, 105°)$, $\theta_H^{upp} = \theta_H^{low} = 0$, $L_x = 4$, $L_y = 16$, $Cn = 0.125$, $Pe = 5 \times 10^3$ ($S = 1.414 \times 10^{-2}$).

lines fall into one of the following categorizes (which do not involve or somehow circumvent the grid roughness effect): (1) the problem of interest was steady and the contact line did not move across the grid (e.g., Ref. 40); (2) only the temporal evolution of the (absolute or relative) position of the contact line (which is much smoother than that of the contact line velocity) was reported (e.g., Ref. 53); (3) the temporal evolution of the contact line velocity was shown, but sampled at some frequency, which could possibly hide the oscillation caused by the grid roughness effect (e.g., Ref. 64). Here we would like to mention that Khatavkar, Anderson, and Meijer[53] attributed the nonsmoothness of the contact line velocity in one of their figures (Fig. 8 therein) to the numerical differentiation of the contact line position. We suspect that it might be related to the grid roughness effect. At the same time, we note that it is probable that in some previous studies the ratio W/h was large enough and the grid roughness effect was not quite significant. We also want to highlight that the contact line becomes a *line* in 3D (instead of a *point* in 2D) and there are multiple grid points near/on the boundary that may affect the contact line; therefore, the effect of the grid roughness could be more complex (e.g., in Ref. 64). This surely need further study.

13. Some discussions about the parameters

Some remarks on the parameters in the present work may be useful. First, we assume the two fluids have the same density, $\rho_A = \rho_B = \rho_c$, thus the density ratio is unity. This differs significantly from the liquid-air systems under usual conditions, in which the liquid/air density ratio can be as high as 10^3. At the same time, this setting is fairly close to some liquid-liquid systems under usual conditions. For instance, Mugele, Baret, and Steinhauser[65] used droplets of water-glycerol-NaCl mixtures with densities about 1000 kg/m^3 in silicone oil (Wacker AK5 with a density about 920 kg/m^3) in their experiments. And recently, Oldenziel, Delfos, and Westerweel[66] used two-fluid systems composed of water/glucose syrup mixture with densities about 1170 kg/m^3 and silicone oil (of three different types, Wacker AK5, AK20, and AK50 with their densities being about 920 kg/m^3, 945 kg/m^3, and 960 kg/m^3, respectively). Besides, for some cases with low Reynolds numbers the inertial effects may be negligible, making the density ratio not so important. Of course, this may not hold for all of the cases studied here, and for cases with intermediate (or even higher) Re the effects of density ratio may be worth pursuing (this is left for future work). Second, we compare some parameters in the experiments by Mugele, Baret, and Steinhauser[65] and Oldenziel, Delfos, and Westerweel[66] for some real liquid-liquid systems with the present work (only one case selected for each work). The comparisons are given in Table I. Note that the drop radius in Ref. 65 was estimated from the drop volume given in that article. The comparisons are made just to show the connections (in terms of the fluid properties and key dimensionless parameters) between the present numerical simulation and the real world while we are aware that the three pieces of work study quite different drop problems. In Table I the fluid properties (e.g., the density, viscosity, interfacial tension and drop

TABLE I. Parameters in the experiments by Mugele, Baret, and Steinhauser,[65] by Oldenziel, Delfos, and Westerweel,[66] and in the present work. Note that only one case in each work is selected for comparison.

Parameter\Source	Ref. 65	Ref. 66	Present
Drop density (kg/m^3)	1000	920	1000
Drop viscosity (dynamic) (mPa s)	5	5.5	5
Ambient fluid density (kg/m^3)	920	1170	1000
Ambient fluid viscosity (dynamic) (mPa s)	5	5.8	5
Interfacial rension (mN/m)	34	21	25
Drop radius (mm)	0.7	3.6	0.4
Density ratio ($-$)	1.09	0.79	1.0
Viscosity ratio (dynamic) ($-$)	1.0	0.95	1.0
Characteristic velocity U_c (m/s)	6.8	3.82	5.0
Characteristic time T_c (s)	1.03×10^{-4}	9.43×10^{-4}	8×10^{-5}
Reynolds number Re ($-$)	952	2299	400
Ohnesorge number Oh ($-$)	0.032	0.021	0.05

radius) in the present work are not uniquely determined; they are just one of the possible sets that would render a Reynolds number of $Re = \sigma R/(\rho_c v_A^2) = 400$.

IV. CONCLUDING REMARKS

To summarize, we have investigated through numerical simulations a 2D drop on a wall with a stepwise WG specified by two distinct contact angles under a broad range of conditions, covering different Reynolds numbers and viscosity ratios, different magnitudes of WG and CAH. Several important issues, including the convergence towards the sharp interface limit, the effect of initial relaxation of the order parameter field, the mechanism of CL slip, and the grid roughness effect, have been examined carefully to establish a solid foundation for the present numerical investigation and also to illustrate certain limitations of the present work. The major findings are summarized as follows. Almost under all conditions (except when the CAH is sufficiently large), the drop was accelerated in the initial stage and gradually reached a steady state. The input Reynolds number (based on the physical properties of the fluids and the drop dimension) was found to have little effect on the capillary number of the drop in steady state. The steady capillary number increases with the viscosity ratio significantly when the viscosity ratio is small, but its dependence on the viscosity ratio becomes weaker at large viscosity ratios. Besides, this capillary number shows linear dependence on the magnitude of the WG under most situations. In the presence of CAH, the motion of the drop is largely determined by the advancing CA of the more hydrophilic region and the receding CA of the more hydrophobic region. When the hysteresis is high enough, the drop remains static because it is within the range of possible configurations allowed by the advancing and receding CAs of both regions. When the initial CA of the drop is larger than the receding CA of the more hydrophobic region or smaller than the advancing CA of the more hydrophilic region, CL pinning in one region may occur during the initial stage. What is more, it has been uncovered that, during its steady motion, the drop assumes a shape that can be well fitted by two arcs corresponding to two different apparent CAs. Besides, in accordance with previous findings by Yue, Zhou, and Feng,[27] the slip length for the WG-driven drop was found to be also proportional to the diffusion length determined by the viscosity and mobility. With a suitably defined slip length, the apparent CAs, the CAs specified on the wall, and the capillary numbers based on the corresponding CL velocities have been found to follow the relation derived by Cox[23] reasonably well. In future, an important further step should be the extension of both the model and investigations to 3D cases. The 2D problems with CAH are relatively simple and the WG in the presence of CAH may be characterized by an equivalent parameter straightforwardly. However, it will not be as easy for 3D problems; it remains to be explored whether such an equivalent parameter exists, and if so, how it can expressed in terms of other known parameters.

ACKNOWLEDGMENTS

[1] A. A. Darhuber and S. M. Troian, "Principles of microfluidic actuation by modulation of surface stresses," Annu. Rev. Fluid Mech. **37**, 425 (2005).

[2] Y.-H. Lai, M.-H. Hsu, and J.-T. Yang, "Enhanced mixing of droplets during coalescence on a surface with a wettability gradient," Lab Chip **10**, 3149–3156 (2010).

[3] H. K. Bardaweel, K. Zamuruyev, J.-P. Delplanque, and C. E. Davis, "Wettability-gradient-driven micropump for transporting discrete liquid drops," J. Micromech. Microeng. **23**, 035036 (2013).

[4] M. J. Hancock, K. Sekeroglu, and M. C. Demirel, "Bioinspired directional surfaces for adhesion, wetting, and transport," Adv. Funct. Mater. **22**, 2223–2234 (2012).

[5] F. Brochard, "Motions of droplets on solid surfaces induced by chemical or thermal gradients," Langmuir **5**, 432–438 (1989).

[6] R. S. Subramanian, N. Moumen, and J. B. McLaughlin, "Motion of a drop on a solid surface due to a wettability gradient," Langmuir **21**, 11844–11849 (2005).

[7] L. M. Pismen and U. Thiele, "Asymptotic theory for a moving droplet driven by a wettability gradient," Phys. Fluids **18**, 042104 (2006).

[8] J. D. Halverson, C. Maldarelli, A. Couzis, and J. Koplik, "A molecular dynamics study of the motion of a nanodroplet of pure liquid on a wetting gradient," J. Chem. Phys. **129**, 164708 (2008).

[9] J. Huang, C. Shu, and Y. Chew, "Numerical investigation of transporting droplets by spatiotemporally controlling substrate wettability," J. Colloid Interface Sci. **328**, 124–133 (2008).

[10] Z.-Y. Shi, G.-H. Hu, and Z.-W. Zhou, "Lattice Boltzmann simulation of droplet motion driven by gradient of wettability," Acta Phys. Sin. **59**, 2595–2600 (2010).

[11] F. D. D. Santos and T. Ondarcuhu, "Free-running droplets," Phys. Rev. Lett. **75**, 2972–2975 (1995).

[12] A. K. Das and P. K. Das, "Multimode dynamics of a liquid drop over an inclined surface with a wettability gradient," Langmuir **26**, 9547–9555 (2010).

[13] X. Xu and T. Qian, "Droplet motion in one-component fluids on solid substrates with wettability gradients," Phys. Rev. E **85**, 051601 (2012).

[14] E. Esmaili, A. Moosavi, and A. Mazloomi, "The dynamics of wettability driven droplets in smooth and corrugated microchannels," J. Stat. Mech. (2012) P10005.

[15] T. Ondarcuhu and M. Veyssie, "Dynamics of spreading of a liquid drop across a surface chemical discontinuity," J. Phys. II **1**, 75–85 (1991).

[16] M. K. Chaudhury and G. M. Whitesides, "How to make water run uphill," Science **256**, 1539–1541 (1992).

[17] N. Moumen, R. S. Subramanian, and J. B. McLaughlin, "Experiments on the motion of drops on a horizontal solid surface due to a wettability gradient," Langmuir **22**, 2682–2690 (2006).

[18] G. C. H. Mo, W. Liu, and D. Y. Kwok, "Surface-ascension of discrete liquid drops via experimental reactive wetting and lattice Boltzmann simulation," Langmuir **21**, 5777–5782 (2005).

[19] R. Yamada and H. Tada, "Manipulation of droplets by dynamically controlled wetting gradients," Langmuir **21**, 4254–4256 (2005).

[20] F. Varnik, P. Truman, B. Wu, P. Uhlmann, D. Raabe, and M. Stamm, "Wetting gradient induced separation of emulsions: A combined experimental and lattice Boltzmann computer simulation study," Phys. Fluids **20**, 072104 (2008).

[21] S. Daniel and M. K. Chaudhury, "Rectified motion of liquid drops on gradient surfaces induced by vibration," Langmuir **18**, 3404–3407 (2002).

[22] S. Daniel, S. Sircar, J. Gliem, and M. K. Chaudhury, "Ratcheting motion of liquid drops on gradient surfaces," Langmuir **20**, 4085–4092 (2004).

[23] R. G. Cox, "The dynamics of the spreading of liquids on a solid surface. Part 1. viscous flow," J. Fluid Mech. **168**, 169–194 (1986).

[24] R. G. Cox, "Inertial and viscous effects on dynamic contact angles," J. Fluid Mech. **357**, 249–278 (1998).

[25] M. Fermigier and P. Jenffer, "An experimental investigation of the dynamic contact angle in liquid-liquid systems," J. Colloid Interface Sci. **146**, 226–241 (1991).

[26] H. Ding, E. Q. Li, F. H. Zhang, Y. Sui, P. D. M. Spelt, and S. T. Thoroddsen, "Propagation of capillary waves and ejection of small droplets in rapid droplet spreading," J. Fluid Mech. **697**, 92–114 (2012).

[27] P. Yue, C. Zhou, and J. J. Feng, "Sharp-interface limit of the Cahn-Hilliard model for moving contact lines," J. Fluid Mech. **645**, 279–294 (2010).

[28] Y. Sui and P. D. M. Spelt, "Validation and modification of asymptotic analysis of slow and rapid droplet spreading by numerical simulation," J. Fluid Mech. **715**, 283–313 (2013).

[29] H. Liu, S. Krishnan, S. Marella, and H. Udaykumar, "Sharp interface Cartesian grid method II: A technique for simulating droplet interactions with surfaces of arbitrary shape," J. Comput. Phys. **210**, 32–54 (2005).

[30] P. D. M. Spelt, "Shear flow past two-dimensional droplets pinned or moving on an adhering channel wall at moderate Reynolds numbers: A numerical study," J. Fluid Mech. **561**, 439 (2006).

[31] C. Fang, C. Hidrovo, F. min Wang, J. Eaton, and K. Goodson, "3-D numerical simulation of contact angle hysteresis for microscale two phase flow," Int. J. Multiphase Flow **34**, 690–705 (2008).

[32] H. Ding and P. D. M. Spelt, "Onset of motion of a three-dimensional droplet on a wall in shear flow at moderate Reynolds numbers," J. Fluid Mech. **599**, 341–362 (2008).

[33] J.-B. Dupont and D. Legendre, "Numerical simulation of static and sliding drop with contact angle hysteresis," J. Comput. Phys. **229**, 2453–2478 (2010).

[34] L. Wang, H. Huang, and X.-Y. Lu, "Scheme for contact angle and its hysteresis in a multiphase lattice Boltzmann method," Phys. Rev. E **87**, 013301 (2013).

[35] J.-J. Huang, H. Huang, C. Shu, Y. T. Chew, and S.-L. Wang, "Hybrid multiple-relaxation-time lattice-Boltzmann finite-difference method for axisymmetric multiphase flows," J. Phys. A: Math. Theor. **46**, 055501 (2013).

[36] J. J. Huang, C. Shu, and Y. T. Chew, "Mobility-dependent bifurcations in capillarity-driven two-phase fluid systems by using a lattice Boltzmann phase-field model," Int. J. Numer. Meth. Fluids **60**, 203–225 (2009).

[37] D. Jacqmin, "Calculation of two-phase Navier-Stokes flows using phase-field modeling," J. Comput. Phys. **155**, 96–127 (1999).

[38] D. Jacqmin, "Contact-line dynamics of a diffuse fluid interface," J. Fluid Mech. **402**, 57–88 (2000).

[39] T. Qian, X.-P. Wang, and P. Sheng, "Molecular scale contact line hydrodynamics of immiscible flows," Phys. Rev. E **68**, 016306 (2003).

[40] A. J. Briant and J. M. Yeomans, "Lattice Boltzmann simulations of contact line motion. II. Binary fluids," Phys. Rev. E **69**, 031603 (2004).

[41] H. Ding and P. D. M. Spelt, "Wetting condition in diffuse interface simulations of contact line motion," Phys. Rev. E **75**, 046708 (2007).

[42] L. Liu and T. Lee, "Wall free energy based polynomial boundary conditions for non-ideal gas lattice Boltzmann equation," Int. J. Mod. Phys. C **20**, 1749–1768 (2009).

[43] A. Carlson, M. Do-Quang, and G. Amberg, "Modeling of dynamic wetting far from equilibrium," Phys. Fluids **21**, 121701 (2009).

[44] H. S. Wiklund, S. B. Lindstrom, and T. Uesaka, "Boundary condition considerations in lattice Boltzmann formulations of wetting binary fluids," Comput. Phys. Commun. **182**, 2192–2200 (2011).

[45] P. Yue and J. J. Feng, "Wall energy relaxation in the Cahn-Hilliard model for moving contact lines," Phys. Fluids **23**, 012106 (2011).

[46] J.-J. Huang, H. Huang, and X. Wang, "Wetting boundary conditions in phase-field-based simulation of binary fluids: Some comparative studies and new development," preprint arXiv:1310.8412 [physics.flu-dyn] (2013).

[47] H. Kusumaatmaja and J. M. Yeomans, "Modeling contact angle hysteresis on chemically patterned and superhydrophobic surfaces," Langmuir **23**, 6019–6032 (2007).

[48] T. Lee and L. Liu, "Lattice Boltzmann simulations of micron-scale drop impact on dry surfaces," J. Comput. Phys. **229**, 8045–8063 (2010).

[49] Y. Q. Zu and S. He, "Phase-field-based lattice Boltzmann model for incompressible binary fluid systems with density and viscosity contrasts," Phys. Rev. E **87**, 043301 (2013).

[50] V. E. Badalassi, H. D. Ceniceros, and S. Banerjee, "Computation of multiphase systems with phase field models," J. Comput. Phys. **190**, 371–397 (2003).

[51] P. Yue, C. Zhou, J. J. Feng, C. F. Ollivier-Gooch, and H. H. Hu, "Phase-field simulations of interfacial dynamics in viscoelastic fluids using finite elements with adaptive meshing," J. Comput. Phys. **219**, 47–67 (2006).

[52] A. V. Coward, Y. Y. Renardy, M. Renardy, and J. R. Richards, "Temporal evolution of periodic disturbances in two-layer Couette flow," J. Comput. Phys. **132**, 346–361 (1997).

[53] V. V. Khatavkar, P. D. Anderson, and H. E. H. Meijer, "Capillary spreading of a droplet in the partially wetting regime using a diffuse-interface model," J. Fluid Mech. **572**, 367–387 (2007).

[54] A. L. Yarin, "Drop impact dynamics: Splashing, spreading, receding, bouncing..." Annu. Rev. Fluid Mech. **38**, 159–192 (2006).

[55] W. Villanueva and G. Amberg, "Some generic capillary-driven flows," Int. J. Multiphase Flow **32**, 1072–1086 (2006).

[56] H. Huang and X.-Y. Lu, "Relative permeabilities and coupling effects in steady-state gas-liquid flow in porous media: A lattice Boltzmann study," Phys. Fluids **21**, 092104 (2009).

[57] Y. Ba, H. Liu, J. Sun, and R. Zheng, "Color-gradient lattice Boltzmann model for simulating droplet motion with contact-angle hysteresis," Phys. Rev. E **88**, 043306 (2013).

[58] A. D. Schleizer and R. T. Bonnecaze, "Displacement of a two-dimensional immiscible droplet adhering to a wall in shear and pressure-driven flows," J. Fluid Mech. **383**, 29–54 (1999).

[59] Cargille immersion oil specifications, Cargille-Sacher Laboratories Inc., Cedar Grove, NJ (2014), see http://www.cargille.com/immeroilspecs.shtml.

[60] H. Ding, P. D. M. Spelt, and C. Shu, "Diffuse interface model for incompressible two-phase flows with large density ratios," J. Comput. Phys. **226**, 2078–2095 (2007).

[61] P. Yue, C. Zhou, and J. J. Feng, "Spontaneous shrinkage of drops and mass conservation in phase-field simulations," J. Comput. Phys. **223**, 1–9 (2007).

[62] Z. Li, G.-H. Hu, Z.-L. Wang, Y.-B. Ma, and Z.-W. Zhou, "Three dimensional flow structures in a moving droplet on substrate: A dissipative particle dynamics study," Phys. Fluids **25**, 072103 (2013).

[63] C. Huh and L. E. Scriven, "Hydrodynamic model of steady movement of a solid/liquid/fluid contact line," J. Colloid Interface Sci. **35**, 85–101 (1971).

[64] X. Jia, J. McLaughlin, and K. Kontomaris, "Lattice Boltzmann simulations of contact line motion on uniform surfaces," Math. Comput. Simul. **72**, 156–159 (2006).

[65] F. Mugele, J.-C. Baret, and D. Steinhauser, "Microfluidic mixing through electrowetting-induced droplet oscillations," Appl. Phys. Lett. **88**, 204106 (2006).

[66] G. Oldenziel, R. Delfos, and J. Westerweel, "Measurements of liquid film thickness for a droplet at a two-fluid interface," Phys. Fluids **24**, 022106 (2012).